The Astrophysical Journal, 834:149 (19pp), 2017 January 10 doi:10.3847/1538-4357/834/2/149

THE EVOLUTION OF GAS GIANT ENTROPY DURING FORMATION BY RUNAWAY ACCRETION

David Berardo[1,2], Andrew Cumming[1,2], and Gabriel-Dominique Marleau[3]
[1] Department of Physics and McGill Space Institute, McGill University, 3550 rue University, Montreal, QC, H3A 2T8, Canada; david.berardo@mcgill.ca
[2] Institut de recherche sur les exoplanètes (iREx), Montreal, QC, Canada; andrew.cumming@mcgill.ca
[3] Physikalisches Institut, Universität Bern, Sidlerstrasse 5, 3012 Bern, Switzerland; gabriel.marleau@space.unibe.ch
Received 2016 July 8; revised 2016 November 18; accepted 2016 November 21; published 2017 January 11

ABSTRACT

We calculate the evolution of gas giant planets during the runaway gas accretion phase of formation, to understand how the luminosity of young giant planets depends on the accretion conditions. We construct steady-state envelope models, and run time-dependent simulations of accreting planets with the code Modules for Experiments in Stellar Astrophysics. We show that the evolution of the internal entropy depends on the contrast between the internal adiabat and the entropy of the accreted material, parametrized by the shock temperature T_0 and pressure P_0. At low temperatures ($T_0 \lesssim$ 300–1000 K, depending on model parameters), the accreted material has a lower entropy than the interior. The convection zone extends to the surface and can drive a high luminosity, leading to rapid cooling and cold starts. For higher temperatures, the accreted material has a higher entropy than the interior, giving a radiative zone that stalls cooling. For $T_0 \gtrsim 2000$ K, the surface–interior entropy contrast cannot be accommodated by the radiative envelope, and the accreted matter accumulates with high entropy, forming a hot start. The final state of the planet depends on the shock temperature, accretion rate, and starting entropy at the onset of runaway accretion. Cold starts with $L \lesssim 5 \times 10^{-6}\ L_\odot$ require low accretion rates and starting entropy, and the temperature of the accreting material needs to be maintained close to the nebula temperature. If instead the temperature is near the value required to radiate the accretion luminosity, $4\pi R^2 \sigma T_0^4 \sim (GM\dot{M}/R)$, as suggested by previous work on radiative shocks in the context of star formation, gas giant planets form in a hot start with $L \sim 10^{-4}\ L_\odot$.

Key words: planets and satellites: formation – planets and satellites: gaseous planets – planets and satellites: physical evolution

1. INTRODUCTION

The direct detection of young gas giant planets is an important test of planet formation mechanisms because the planet has had less time to thermally relax at young ages, and therefore its thermal state depends on how it formed (Stevenson 1982; Fortney et al. 2005, 2008; Marley et al. 2007). Traditional cooling models for brown dwarfs and giant planets were based on hot initial (post-formation) conditions, in which case the thermal time is short and the planet quickly forgets the initial conditions and evolves onto a cooling track that only depends on the mass (e.g., Burrows et al. 1997; Baraffe et al. 2003). Fortney et al. (2005) and Marley et al. (2007) pointed out that gas giants that formed by core accretion might be much colder than these earlier "hot-start" models. They showed that the core accretion model described in the series of papers of Pollack et al. (1996), Bodenheimer et al. (2000), and Hubickyj et al. (2005) produced planets that were significantly less luminous, implying that giant planets instead have a "cold start."

Given uncertainties in planet formation models and the potentially wide range in luminosity of newly formed gas giant planets, Spiegel & Burrows (2012) took the approach of treating the internal entropy of the gas giant after formation as a free parameter, producing a range of "warm starts." The predicted cooling tracks then depend on the planet mass and initial entropy. Bonnefoy et al. (2013) and Marleau & Cumming (2014) explored the joint constraint on these two parameters that can be inferred from a directly imaged planet with a known luminosity and age. For hot initial conditions, the cooling tracks only depend on the mass; cold initial conditions require a more massive planet to match the observed luminosity. Fitting hot-start cooling curves therefore gives a lower limit on the planet mass. Matching the observed luminosity gives a lower limit on the initial entropy because luminosity sensitively depends on the internal entropy (e.g., Figure 2 of Marleau & Cumming 2014). Additional information about the planet mass, such as an upper limit from dynamics, can break the degeneracy and reduce the allowed range of initial entropy.

The population of directly imaged planets shows a wide range of luminosities (e.g., Neuhäuser & Schmidt 2012; Bowler 2016), with most being too luminous to be cold starts. Examples are β Pic b with $L \approx 2 \times 10^{-4}\ L_\odot$ (Lagrange 2009, 2010; Bonnefoy et al. 2013), or the HR8799 planets with $L \approx 2 \times 10^{-5}\ L_\odot$ for HR8799c, d, and e, and $8 \times 10^{-6}\ L_\odot$ for HR8799b (Marois 2008; Marois et al. 2010). The inferred initial entropies in these cases are significantly higher than in Marley et al. (2007) (Bonnefoy et al. 2013; Bowler et al. 2013; Currie et al. 2013; Marleau & Cumming 2014). The best case for a cold start is the young giant planet 51 Eri b, which has a projected separation of 13 au from its star and $L \approx 1.4$–$4 \times 10^{-6}\ L_\odot$ (Macintosh et al. 2015). This luminosity is consistent with the value $\approx 2 \times 10^{-6}\ L_\odot$ predicted by Marley et al. (2007), but it also matches a hot start for a planet mass 2–3 M_J at the stellar age $\approx$20 Myr. Similarly, the low effective temperature of 850 K for HD 131399Ab corresponds to a hot-start mass of 4 M_J at 16 Myr (Wagner et al. 2016). Another cold object is GJ 504b, which has an effective temperature of only 510 K (Kuzuhara et al. 2013), but indications that the star is several Gyr old imply that it may be a low-mass brown dwarf rather than a planet (Fuhrmann & Chini 2015; D'Orazi et al. 2016).

The discovery of protoplanets still embedded in a protoplanetary disk has been interesting from the point of view

of testing formation models. For example, HD 100546 b is a directly imaged object located 50 au away from its Herbig Ae/Be host with a luminosity $\sim 10^{-4}\ L_\odot$ (Quanz et al. 2013; Currie et al. 2014a; Quanz 2015), and the star may host a second planet closer in (Currie et al. 2015; Garufi et al. 2016). Sallum et al. (2015) identified two and perhaps three accreting protoplanets in the transition disk of LkCa 15. The infrared and Hα luminosities were consistent with expected accretion rates: Sallum et al. (2015) report $M\dot{M} \sim 10^{-5}\ M_J^2\ \mathrm{yr}^{-1}$, where M and $\dot{M}$ are the planetary mass and accretion rate, respectively, which agrees with typical accretion rates of $\sim 10^{-3}$–$10^{-2}\ M_\oplus\ \mathrm{yr}^{-1}$ in models (e.g., Lissauer et al. 2009) for $M \sim M_J$. The young ages of these stars $\lesssim$10 Myr correspond to early times when there is greater potential for distinguishing formation models (e.g., Figure 4 of Marley et al. 2007), especially since the planets could be substantially younger than the star (Fortney et al. 2005). The observations are difficult to interpret, however. Contributions from the environment around the protoplanet, which is likely still accreting, need to be considered, and if accretion is ongoing, the accretion luminosity $L_{\rm accr} \approx GM\dot{M}/R$, where R is the planetary radius, may dominate the internal luminosity. Nevertheless, these effects can potentially be distinguished by studying the spectral energy distribution or by spatially resolving the emission. For example, observations of HD 100546 b are able to make out a point-source component (surrounded by spatially resolved emission) with a blackbody radius and luminosity consistent with those of a young gas giant (Currie et al. 2014b; Quanz 2015).

Interpreting the current and upcoming observations of young gas giants requires a better understanding of the physics that sets the thermal state of the planet during and immediately after formation. Marley et al. (2007) emphasized that because most of the mass of the gas giant is delivered through an accretion shock, the efficiency with which the shock radiates away the gravitational energy of the accreted matter is a key uncertainty that determines the temperature of the material that is added to the planet by accretion. The need to accurately treat the radiative cooling at the shock (in particular whether the shock is supercritical, e.g., see Commerçon et al. 2011) has been discussed in Section 8.1 of Mordasini et al. (2012) and in reviews such as Chabrier et al. (2014, p. 619). Mordasini (2013) also identified the planetesimal surface density in the disk as a key ingredient since it sets the core mass. He simulated the growth of planets under cold- and hot-start conditions by changing the outer boundary condition for the planet during the accretion phase. In the cold case, the final entropy of the planet was found to sensitively depend on the resulting core mass through the feedback action of the accretion shock. Most recently, Owen & Menou (2016) pointed out the potential importance of non-spherical accretion and studied the role of an accretion boundary layer in setting the thermal state of the accreted matter.

In this paper, we focus on the phase of the core accretion scenario in which the accreting matter forms a shock at the surface of the planet. This runaway accretion phase occurs once the contraction rate of the gas envelope surrounding a newly formed core of $\sim 10\ M_\oplus$ becomes higher than the rate at which the disk can supply mass to the envelope (e.g., Helled et al. 2014, p. 643; Mordasini et al. 2015). The planet then shrinks within its Hill sphere and mass flows hydrodynamically onto the planet. Given the uncertainty in the temperature of the post-shock material, we treat the entropy at the surface of the planet as a free parameter. The aim is to better understand how the matter deposited by the accretion shock becomes part of the planet and therefore sets the internal entropy. This approach is similar to previous work on accreting protostars in which the efficiency of the accretion shock is treated as a free parameter (e.g., Prialnik & Livio 1985; Siess et al. 1997; Baraffe et al. 2009; see discussion in Section 2.1). We improve on the previous calculations of core accretion with hot outer boundaries by Mordasini et al. (2012) and Mordasini (2013), which assumed constant luminosity inside the planet and only global energy conservation, by following the full internal energy profile during accretion.

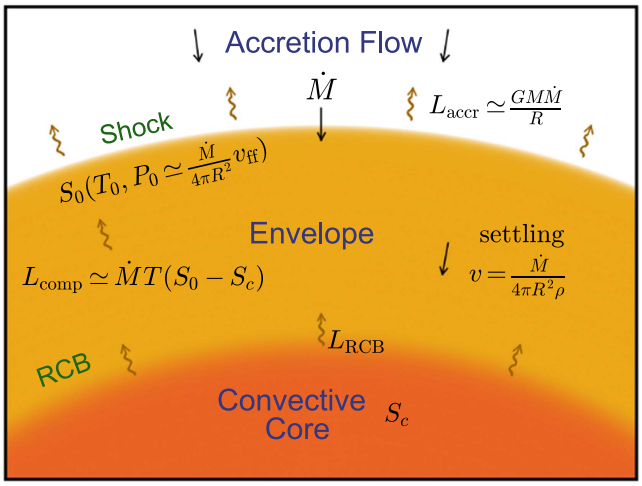

Figure 1. Diagram of a spherically symmetrically accreting gas giant. Shown are the last parts of the accretion flow (top), the radiative envelope (middle), and the convective interior (bottom). Matter accretes onto the envelope with a rate $\dot{M}$, where it shocks and releases energy as an accretion luminosity $L_{\rm accr}$. Immediately after the shock, the matter has temperature T_0, pressure P_0 equal to the ram pressure (Equation (3)), and thus entropy S_0. As the material settles down through the envelope to the convective core with a velocity $v = \dot{M}/4\pi r^2 \rho$, it releases an additional luminosity $L_{\rm comp}$ from compressional heating and finally reaches the radiative-convective boundary (RCB). The convective core has entropy S_c and supplies a luminosity $L_{\rm RCB}$ to the base of the envelope.

A schematic diagram of the different regions we consider in this paper is shown in Figure 1. We start in Section 2 by discussing the expected values of entropy of the accreted material deposited by the accretion shock at the surface of the planet. In Section 3 we compute thermal steady-state models of the accreting envelope to understand how freshly accreted material becomes part of the planet, following Stahler (1988), who studied the envelopes of accreting low-mass protostars. We show that there are three regimes of accretion that depend on how the entropy of the newly accreted material compares to the internal adiabat. In Section 4 we numerically calculate the evolution of gas giants that accrete matter with a range of entropy, using the code Modules for Experiments in Stellar Astrophysics (MESA) (Paxton et al. 2011, 2013, 2015), and investigate the sensitivity of the final thermal state of the planet to the shock conditions and starting entropy at the onset of accretion. We summarize, compare our results to observed systems, and discuss the implications in Section 5. Finally, analytical formulæ for the entropy of an ideal gas as well as analytic solutions of envelope structures of accreting atmospheres are presented in Appendices A and B, respectively.

2. ENTROPY OF THE POST-SHOCK GAS

In this section, we discuss the state of the gas immediately after the accretion shock.

2.1. Previous Approaches to Hot and Cold Accretion

There have been a few different approaches in the literature to modeling the unknown radiative efficiency of the accretion shock in accreting protostars and planets. This results in different assumptions about the post-shock temperature and entropy (S_0 and T_0 in Figure 1).

In the context of gas giant formation, the core accretion models of Pollack et al. (1996), Bodenheimer et al. (2000), and Hubickyj et al. (2005) are based on the assumption that the shock is isothermal, with a temperature set by integrating the radiative diffusion equation inwards through the spherical accretion flow from the nebula (i.e., the local circumstellar disk) to the shock. In the limit where the flow is optically thin, the shock temperature is then the nebula temperature, but could be much higher if the flow is optically thick (see discussion in Section 2 of Bodenheimer et al. 2000). The cold accretion limit of these models is therefore that the post-shock temperature of the gas is $T_0 = T_{\rm neb}$, or 150 K in the calculations of Hubickyj et al. (2005) (although whether the temperatures in the models corresponding to the Marley et al. 2007 cold starts were that low was not explicitly reported).

An alternative approach that has been used in a variety of contexts is to model the shock efficiency by the fraction of the specific accretion energy GM/R that is incorporated into the star or planet. This is implemented either by adding an amount $\alpha GM/R$ to the specific internal energy of the accreted matter if following the detailed structure with a stellar evolution code (Prialnik & Livio 1985; Siess et al. 1997; Baraffe et al. 2009), or by adding a contribution $\alpha GM\dot{M}/R$ to the luminosity if following the global energetics (Hartmann et al. 1997). For gas giant accretion, Mordasini et al. (2012) and Mordasini (2013) step through sequences of detailed planet models by tracking the global energetics, and model cold or hot accretion by excluding or including the accretion luminosity in the internal luminosity of the planet. Owen & Menou (2016) recently applied the approach of Hartmann et al. (1997) to disk-fed planetary growth, calculating α as set by the disk boundary layer.

In these approaches, the cold limit corresponds to setting $\alpha = 0$, which means that the accreting material adjusts its temperature to match the gas that is already at the surface. With this boundary condition, the cooling history of the accreting object is affected by accretion only through the fact that its mass is growing, which changes its thermal timescale. Even for $\alpha = 0$, the temperature at the surface can be much higher than $T_{\rm neb}$, and so this is a different cold limit than in Bodenheimer et al. (2000). For example, taking a typical internal luminosity $L_{\rm int} \sim 10^{-4}\, L_\odot$ and planet radius $2\, R_J$ gives $T_0 = T_{\rm therm} \approx (L_{\rm int}/4\pi R^2\sigma)^{1/4} \approx 1300$ K, where σ is the Stefan–Boltzmann constant.

In the hot limit with $\alpha = 1$, the surface temperature is given by $T_0 = T_{\rm hot} \approx (L_{\rm accr}/4\pi R^2\sigma)^{1/4}$, where $L_{\rm accr} \approx GM\dot{M}/R$ is the accretion luminosity,

$$L_{\rm accr} \approx 4.4 \times 10^{-3}\, L_\odot \left(\frac{\dot{M}}{10^{-2}\, M_\oplus\ {\rm yr}^{-1}}\right)\left(\frac{M}{M_J}\right)\left(\frac{R}{2\, R_J}\right)^{-1}. \quad (1)$$

This gives a temperature

$$T_{\rm hot} \approx 3300\ {\rm K} \left(\frac{\dot{M}}{10^{-2}\, M_\oplus\ {\rm yr}^{-1}}\right)^{1/4}\left(\frac{M}{M_J}\right)^{1/4}\left(\frac{R}{2\, R_J}\right)^{-3/4}. \quad (2)$$

We have scaled to a typical accretion rate during the runaway accretion phase of $\dot{M} \lesssim 10^{-2}\, M_\oplus\ {\rm yr}^{-1} = 1.9 \times 10^{18}$ g s^{-1} (Pollack et al. 1996; Lissauer et al. 2009) and use as everywhere $R_J = 7.15 \times 10^9$ cm.

Shock models suggest that the post-shock temperature is more likely to be close to $T_{\rm hot}$ than $T_{\rm neb}$. Stahler et al. (1980) argued that even if the accretion flow is optically thin, the outer layers of the protostar (or here the planet) will be heated because some of the energy released in the shock is radiated inwards (see Figure 5 of Stahler et al. 1980 and associated discussion; see also the discussion in Calvet & Gullbring 1998 and Commerçon et al. 2011). For an optically thin accretion flow, Stahler et al. (1980) derived the relation $4\pi R^2\sigma T^4 \approx (3/4)L_{\rm accr}$ for the post-shock temperature (see their Equation (24)), which is $(3/4)^{1/4}T_{\rm hot} \approx 3100$ K. The factor of $3/4$ relies on an approximate estimate of the outward radiation that is reprocessed and travels back inwards toward the surface, but the temperature is only weakly affected (for example, a factor $1/4$ would still give 2300 K). This suggests that the temperature in the post-shock layers is $T_0 \gg T_{\rm neb}$ and even $T_0 \gg T_{\rm therm}$. However, since detailed calculations of the radiative transfer associated with the shock are in their early stages (e.g., Marleau et al. 2016), we will treat T_0 as a free parameter and consider values in the full range from $\approx T_{\rm neb}$ to $\approx T_{\rm hot}$.

2.2. The Physical Conditions Post-shock

We now discuss the conditions post-shock, taking the temperature T_0 as a parameter. Following Bodenheimer et al. (2000), we consider an isothermal shock with density jump $\rho_2/\rho_1 = v_{\rm ff}^2/c_s^2$, where the matter arrives at the free-fall velocity $v_{\rm ff} = (2GM/R)^{1/2} = 42$ km s^{-1} $(M/M_J)^{1/2}(2\, R_J/R)^{1/2}$, and c_s is the isothermal sound speed. The post-shock pressure is the ram pressure $P_{\rm accr} = \rho_2 c_s^2 = \dot{M}v_{\rm ff}/4\pi R^2$ or

$$P_{\rm accr} = 3.1 \times 10^3\ {\rm erg\ cm^{-3}} \left(\frac{\dot{M}}{10^{-2}\, M_\oplus\ {\rm yr}^{-1}}\right) \times \left(\frac{M}{M_J}\right)^{1/2}\left(\frac{R}{2\, R_J}\right)^{-5/2}. \quad (3)$$

(Note that we use cgs units for pressure here; we recall that $P = 1$ bar $= 10^6$ erg cm^{-3}.)

At the low densities near the surface of the planet, the equation of state is close to an ideal gas. In Appendix A we show that for a mixture of H_2 and He with a helium mass fraction $Y = 0.243$ (matching the value used by Pollack et al. 1996), the entropy[4] per baryon is

$$\frac{S}{k_{\rm B}/m_p} \approx 10.8 + 3.4\log_{10}T_3 - 1.0\log_{10}P_4, \quad (4)$$

[4] Throughout this work, entropies have the same reference point as the published tables of Saumon et al. (1995), and hence can be directly compared to the MESA code and Marleau & Cumming (2014). When comparing to other works, it is important to note that a different reference point may have been chosen (see Figure 4 and Appendix B of Marleau & Cumming 2014).

where k_B is Boltzmann's constant, m_p is the proton mass, and $T_3 \equiv T/(1000\ \mathrm{K})$, $P_4 \equiv P/(10^4\ \mathrm{erg\ cm^{-3}})$. Using the ram pressure (Equation (3)) and assuming the gas remains molecular post-shock, the post-shock entropy S_0 is therefore

$$\frac{S_0}{k_B/m_p} \approx 7.4 - \log_{10}\left(\frac{\dot{M}}{10^{-2}\ M_\oplus\ \mathrm{yr}^{-1}}\right) + 3.4\log_{10}\left(\frac{T_0}{150\ \mathrm{K}}\right) - 0.51\log_{10}\left(\frac{M}{M_J}\right) + 2.5\log_{10}\left(\frac{R}{2\ R_J}\right), \quad (5)$$

where we have scaled to the lowest possible temperature expected for T_0, which is the nebula temperature in Hubickyj et al. (2005). At higher temperatures, the hydrogen will be atomic post-shock, in which case the entropy is (Appendix A)

$$\frac{S}{k_B/m_p} \approx 17.2 + 4.7\log_{10}T_3 - 1.9\log_{10}P_4. \quad (6)$$

The maximal value of entropy we expect is for $T_0 \approx T_{\mathrm{hot}}$ (Equation (2)), which gives

$$\frac{S_0}{k_B/m_p} \approx 20.6 - 0.72\log_{10}\left(\frac{\dot{M}}{10^{-2}\ M_\oplus\ \mathrm{yr}^{-1}}\right) + 0.23\log_{10}\left(\frac{M}{M_J}\right) + 1.17\log_{10}\left(\frac{R}{2R_J}\right). \quad (7)$$

We see that there is a large variation in S_0, the entropy of the material deposited at the planet surface, depending on the shock temperature. These values can be higher or lower than the internal entropy of the planet at the moment runaway accretion begins (which for example is $S \approx 11\ k_B/m_p$ in the simulations of Mordasini 2013). In the next section we investigate the response of the planet to accretion in these different cases.

3. THE STRUCTURE OF THE ACCRETING ENVELOPE

To understand the evolution of the accreting gas after arrival on the planet, we first construct envelope models following the approach of Stahler et al. (1980) and Stahler (1988) for accreting low-mass protostars. In the envelope, the entropy profile adjusts from the surface value S_0 to the interior value S_c. The thermal timescale across the envelope is shorter than the evolution time, so that we can assume thermal equilibrium for the envelope. Indeed, we show in the time-dependent simulations in the next section that the envelope adopts a self-similar profile, slowly adjusting over longer timescales as the internal entropy changes.

3.1. Envelope Models

We follow Stahler (1988) and construct a plane-parallel envelope model in thermal equilibrium with constant gravity $g = GM/R^2 = 6.2\times10^2\ \mathrm{cm\ s^{-2}}(M/M_J)(R/2\ R_J)^{-2}$. This is a good approximation since the envelope is thin: $H_P/R \approx 0.005\ (T/1000\ \mathrm{K})(R/2\ R_J)(M/M_J)^{-1}(\mu/2)^{-1}$, where $H_P = k_BT/\mu m_p g$ is the pressure scale height and μ the mean molecular weight. The entropy equation is

$$T\frac{\partial S}{\partial t} + vT\frac{\partial S}{\partial r} = -\frac{1}{4\pi r^2\rho}\frac{\partial L}{\partial r}, \quad (8)$$

where $L(r)$ is the luminosity at radius r. Mass continuity gives the velocity of the settling material $v = -\dot{M}/4\pi r^2\rho$. Switching to pressure as an independent coordinate using hydrostatic balance $dP/dr = -\rho g$, and assuming a steady state, Equation (8) becomes

$$\dot{M}T\frac{dS}{dP} = \frac{dL}{dP}. \quad (9)$$

As pointed out by Stahler (1988), this shows that to the extent that temperature is constant, $L - \dot{M}TS$ is constant in the envelope, so that in particular the change in luminosity ΔL across the envelope is related to the change in entropy ΔS as $\Delta L \approx \dot{M}T\Delta S$.

To calculate the envelope models, we rewrite Equation (9), and integrate equations for T and L as a function of pressure,

$$\frac{dT}{dP} = \frac{T}{P}\nabla \quad (10)$$

$$\frac{dL}{dP} = \dot{M}T\left[\left.\frac{\partial S}{\partial P}\right|_T + \left.\frac{\partial S}{\partial T}\right|_P\frac{dT}{dP}\right], \quad (11)$$

where $\nabla = d\ln T/d\ln P$ is the temperature gradient in the planet.[5] We use the equation-of-state tables from the MESA code for our integrations and assume that the composition of the atmosphere is hydrogen and helium with a helium mass fraction $Y = 0.243$ (Pollack et al. 1996). We integrate inwards to a pressure of $10^8\ \mathrm{erg\ cm^{-3}}$, where the density is typically $\sim 3\times10^{-4}\ \mathrm{g\ cm^{-3}}$. Under these conditions, the equation of state is close to an ideal gas (e.g., see Figure 1 of Saumon et al. 1995), and we find similar results assuming an ideal gas equation of state and calculating the dissociation fraction of the molecular hydrogen using the Saha equation, as outlined in Appendix A. The mass and radius of the planet are free parameters in the envelope model. We use the giant planet models of Marleau & Cumming (2014) to self-consistently determine the radius corresponding to the internal entropy of the planet, matching the entropy of the convection zone at the base of the envelope model.

The temperature gradient ∇ depends on the heat transport mechanism. For radiative diffusion, $\nabla = \nabla_{\mathrm{rad}}$ given by the radiative diffusion equation

$$L = -4\pi r^2\frac{4acT^3}{3\kappa\rho}\frac{dT}{dr} = \frac{16\pi acT^4GM}{3\kappa P}\nabla_{\mathrm{rad}}. \quad (12)$$

We calculate the opacity κ using the tables supplied with MESA, choosing the low-temperature tables based on Freedman et al. (2008, 2014) with $Z = 0.02$ (the `lowT_Freedman11_z0.02.data` table). These opacities do not include grain opacity, which is significantly uncertain because small grains may coagulate and settle out of the atmosphere (Podolak 2003; Movshovitz & Podolak 2008). Core accretion models often assume a fixed grain contribution, e.g., 2% of interstellar values Pollack et al. (1996). Movshovitz et al. (2010) modeled grain evolution up to crossover mass and found that the grain opacity was even lower. Mordasini et al. (2014a) and Mordasini (2014b) compared planet population

[5] The code used to calculate the envelope models is available at https://github.com/andrewcumming/gasgiant.

synthesis models with observations, preferring a grain opacity of 0.3% of the interstellar value. In most of the models in this paper, we include only the gas opacity and assume that grain opacity is not significant. We investigate the influence of grain opacity in Section 3.4.

The post-shock material is typically in the free-streaming regime, i.e., it is optically thin over a few post-shock pressure scale heights. Indeed, defining the photosphere to be where the optical depth as measured from the shock $\Delta\tau \approx 1$, the photospheric pressure $P_{\rm phot} \approx g/\kappa$ is higher than the ram pressure $P_{\rm accr}$ by a factor of f times $e \approx 2.7$ when $\kappa \lesssim 0.02$ cm^2 g^{-1} $(f/3)^{-1}(\dot{M}/0.01\ M_\oplus\ {\rm yr}^{-1})(RM/2R_J M_J)^{1/2}$ (see Equation (3)), which is generally satisfied when the grain contribution to the opacity is suppressed to the percent level. We note that $P_{\rm phot} \sim g/\kappa$ holds regardless of the optical thickness of the upstream accretion flow since the post-shock gas is (nearly) in hydrostatic equilibrium, which implies $P \sim \rho \Delta r g$, where Δr is the distance from the shock.

Equation (12) remains valid in free-streaming conditions under the assumptions of a gray opacity, local thermodynamic equilibrium, and the Eddington approximation (e.g., Hubeny & Mihalas 2014). We do not follow energy deposited within the (optically thin) outer layers of the envelope due to irradiation by the accretion shock. Instead, we include the influence of the accretion shock by setting the temperature T_0 at the post-shock ram pressure $P = P_{\rm accr}$. This approach should be valid but could be verified by a detailed calculation of the radiative transfer through the shock and in the outer layers.

When $\nabla_{\rm rad} > \nabla_{\rm ad}$, where $\nabla_{\rm ad} = (\partial \ln T/\partial \ln P)_S$ is the adiabatic gradient, convection transports energy. In that case, we calculate ∇ from mixing length theory following Henyey et al. 1965 (see Hubeny & Mihalas 2014 for a useful summary). For efficient convection, the convective luminosity is

$$L_{\rm conv} = 4\pi R^2 \frac{1}{2} \rho v_{\rm conv} c_P T (\nabla - \nabla_{\rm ad}), \quad (13)$$

where we set the mixing length equal to the pressure scale height, c_P is the heat capacity per unit mass at constant pressure, and the convective velocity is $v_{\rm conv} \approx (gH/8)^{1/2}$ $(\nabla - \nabla_{\rm ad})^{1/2} = (P/8\rho)^{1/2}(\nabla - \nabla_{\rm ad})^{1/2}$. Near the surface of the convection zone, the $\nabla - \nabla_{\rm ad}$ term can be on the order of unity. The convection extends into optically thin ($\Delta\tau \ll 1$) regions of the envelope for low shock temperatures, and radiative losses from convective elements reduce the convective efficiency. We account for this using the prescription of Henyey et al. (1965) using $\Delta\tau$ as the optical depth. It is not clear whether this applies for the situation of a bounded atmosphere that is irradiated by the accretion shock and in which the accretion flow above the shock can be optically thick. However, we find that including radiative losses in the mixing length prescription changes the luminosity in the envelope by less than a few percent.

3.2. Structure of the Envelope for Different Boundary Temperatures

Figure 2 shows example profiles of the accreting envelope for the same accretion rate and internal adiabat, but with different outer boundary temperatures. We model a 1 M_J, 2 R_J planet accreting at 0.01 $M_\oplus$ yr^{-1}. We adjust the luminosity at the top of the atmosphere to try to match the entropy at the base

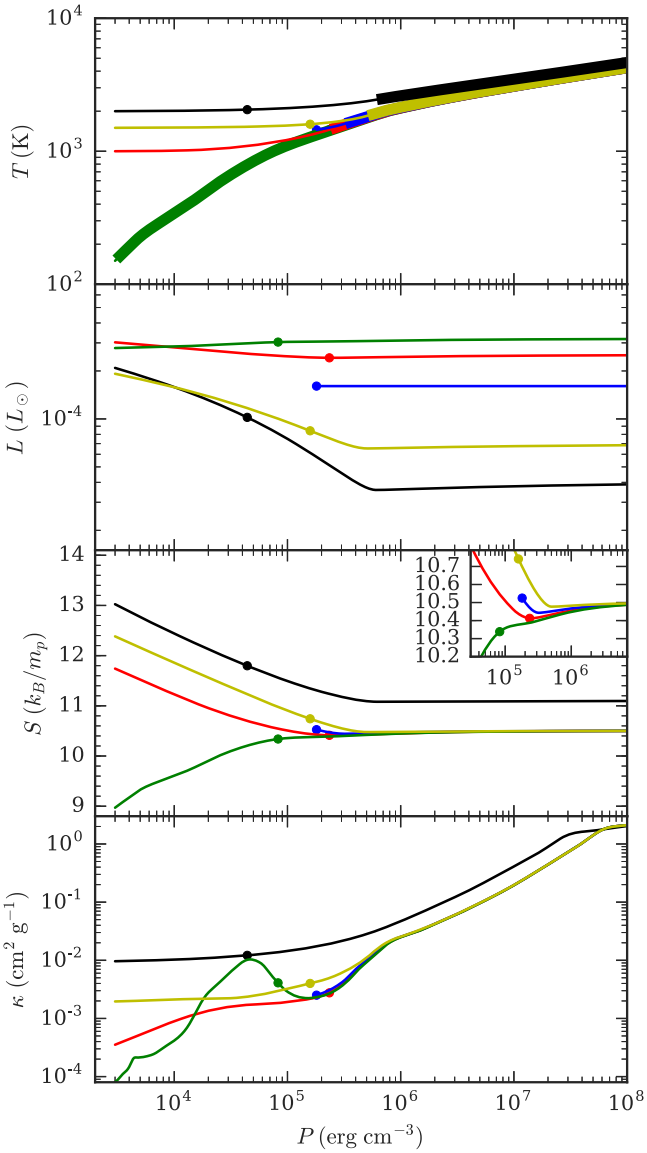

Figure 2. Envelope profile for different choices of outer boundary temperature. The black, yellow, red, and green curves are for outer temperatures $T_0 = 2000$, 1500, 1000, and 150 K at a pressure $P_0 = 3 \times 10^3$ erg cm^{-3}. Except for the hottest model, we have chosen the luminosity of the different envelope models so that they match a convection zone with entropy 10.5 $k_{\rm B}/m_p$ at depth. Blue is for a cooling boundary condition with no accretion. In all cases, the planet has mass 1 M_J and radius 2 R_J. The accretion rate for the accreting envelopes is $\dot{M} = 0.01\ \dot{M}_\oplus$ yr^{-1}. The filled circles show the location where the optical depth from the shock $\Delta\tau = 2/3$. The region of convection is indicated by thick lines in the temperature profiles in the upper panel. The inset shows the region near the radiative-convective boundary.

of the atmosphere at $P = 10^8$ erg cm^{-3} to $S_c = 10.5\ k_{\rm B}/m_p$, the appropriate value of internal entropy for 2 R_J (e.g., Figure A1 of Marleau & Cumming 2014). The outer boundary is placed at the ram pressure, which is 3×10^3 erg cm^{-3} from Equation (3). We also show the envelope profile for an isolated nonaccreting planet for comparison, where we set the outer pressure to $P_{\rm phot} = (2/3)(g/\kappa)$ and set the temperature to $T_{\rm eff} = (L/4\pi R^2 \sigma)^{1/4}$.

We find that the structure and luminosity of the accreting envelope depends on the entropy at the outer boundary. If the surface entropy is significantly higher than the internal entropy, the radiative-convective boundary (RCB) is pushed deeper, and

the luminosity there, $L_{\rm RCB}$, is lower. This is important because $L_{\rm RCB}$ determines how quickly the convective core cools down and moves to lower entropy. The effect of the hot envelope is therefore to reduce the cooling luminosity and increase the cooling timescale of the planet. At lower surface entropy, the material in the envelope reaches lower entropy than the convection zone. This entropy inversion enhances convection, moving the RCB outwards and increasing the cooling luminosity. The models with hotter outer temperatures of 1500 and 2000 K in Figure 2 are examples of envelopes with reduced cooling luminosity.

The entropy and luminosity profiles in the envelope are similar to those considered by Stahler (1988) (see Figure 4 of that paper). The luminosity increases outwards due to compressional heating, which supplies a luminosity $L_{\rm comp} \approx \dot{M} T \Delta S$ or

$$L_{\rm comp} \approx 8 \times 10^{-5}\, L_\odot \left(\frac{\dot{M}}{10^{-2}\, M_\oplus\ {\rm yr}^{-1}}\right) \times \left(\frac{T}{2000\ {\rm K}}\right)\left(\frac{\Delta S}{k_{\rm B}/m_p}\right). \quad (14)$$

The entropy decreases inwards in the radiative zone, joining smoothly onto the convection zone at the RCB. In the convection zone, the entropy initially slightly increases inwards and then levels off as convection becomes efficient and dominates the energy transport. The hot outer boundary pushes the RCB deeper into the planet than in a nonaccreting planet with the same internal entropy. This causes the luminosity to leave the convective core smaller (e.g., Burrows et al. 2000; Arras & Bildsten 2006), so that the core cools more slowly. For the $T_0 = 2000$ K case, the RCB moves inwards by about a factor of 2 in pressure, and the cooling is slower by about a factor of 4 than in a nonaccreting planet.

In the colder model with an outer temperature of 1000 K, the entropy quickly drops below the entropy of the convection zone on moving inwards through the envelope. Convection extends out almost to the photosphere, and the luminosity is higher than in the nonaccreting case. The potential for enhanced luminosity can be understood by considering the entropy gradient in the planet, which is (Stahler 1988)

$$\frac{dS}{d\ln P} = c_P(\nabla - \nabla_{\rm ad}). \quad (15)$$

When $c_P = (7/4)(k_{\rm B}/m_p)$ (assuming pure H_2 with $\mu = 2$ and only translational and rotational degrees of freedom), a change in entropy ΔS across a pressure range $\Delta \log_{10} P$ implies

$$\nabla - \nabla_{\rm ad} \approx 0.25\left(\frac{\Delta S}{k_{\rm B}/m_p}\right)\frac{1}{\Delta \log_{10} P}. \quad (16)$$

This significant departure from adiabaticity near the outer boundary is needed to increase the entropy from its value at the outer edge of the convection zone to the value at the center, S_c. From Equation (13), the luminosity resulting from this superadiabaticity is

$$L_{\rm conv} \sim 10^{-3}\, L_\odot \left(\frac{R}{2\, R_J}\right)^2 \left(\frac{\nabla - \nabla_{\rm ad}}{0.25}\right)^{3/2} \times \left(\frac{T}{1000\ {\rm K}}\right)^{1/2}\left(\frac{P}{10^5\ {\rm erg\ cm^{-3}}}\right). \quad (17)$$

The luminosities of the envelopes with the colder outer boundaries are therefore greater by a factor of 1.5 for $T_0 = 1000$ K than the cooling luminosity of the planet without accretion, and greater by a factor of two for $T_0 = 150$ K, which is convective all the way out to the outer boundary.

3.3. Hot Accretion: A Minimum Luminosity and Minimum Entropy for Hot Envelopes

The hottest model in Figure 2, with $T_0 = 2000$ K, does not match an internal adiabat with $S_c = 10.5\ k_{\rm B}/m_p$. Constructing envelope models with different luminosities, the lowest entropy that we can match with an outward luminosity is $S_c = 11.1\ k_{\rm B}/m_p$, which is the model shown in Figure 2. For lower values of luminosity at the surface, we are not able to find a solution. The temperature reaches a maximum and then exponentially drops on integrating inwards. This was seen in the envelope models of Stahler (1988) (see Figure 2 of that paper). A way to think of this is that the envelope can accommodate a lower luminosity at the surface by reducing the base entropy for high-luminosity envelopes, thereby reducing the luminosity entering the envelope at the base. However, at some point, the only way in which the envelope can accommodate a lower surface luminosity is by sending some of the compressional heating inwards through the lower boundary to the core. In Appendix B we describe an analytic model of the accreting envelope with a power-law opacity that reproduces this behavior and helps to explain why accreting envelopes have a minimum luminosity.

To explore this further, we calculated the minimal entropy $S_{\rm min}$ at the base of the envelope as a function of T_0 and $\dot{M}$. Fixing T_0, we found the minimal-entropy envelope by solving for the luminosity at the surface that gave a vanishing luminosity at the base of the envelope. This solution is equivalent to the critical solution discussed by Stahler (1988); the minimal entropy $S_{\rm min}$ is equivalent to $s_{\rm sett}$ in that paper. Figure 3 shows how $S_{\rm min}$ varies with surface temperature T_0 for different accretion rates for a planet with mass 1 M_J and radius 2 R_J. If the planet has an internal adiabat with $S_c > S_{\rm min}$, the radiative envelope can connect smoothly to the convective interior. This is not the case, however, if $S_c < S_{\rm min}$, implying that the accreted matter will accumulate with a much greater entropy than the internal adiabat. We explore the consequences of this in time-dependent models in Section 4. The value of $S_{\rm min}$ decreases with planet mass, which is shown by the dashed curve in Figure 3, which is for $\dot{M} = 10^{-2}\ M_\oplus\ {\rm yr}^{-1}$, but for a 3 M_J, 1.5 R_J planet. In calculating $S_{\rm min}$, we set the surface pressure to the ram pressure, but we find that $S_{\rm min}$ is not very sensitive to surface pressure (dotted curve in Figure 3).

3.4. Influence of Grain Opacity

To investigate the effect of grain opacity on the envelope, we use two approaches. First, to include the full grain opacity, we use

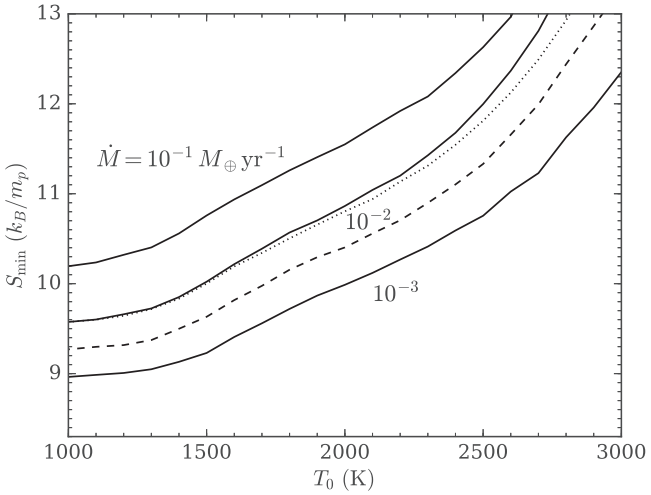

Figure 3. Minimum value of internal entropy to which a radiative envelope can smoothly attach as a function of the outer boundary temperature T_0. The solid curves have the outer boundary pressure set equal to the ram pressure, with $M = 1\ M_J$ and $R = 2\ R_J$; the dotted curve shows the effect of increasing the outer boundary pressure by a factor of 10 for $\dot{M} = 10^{-2}\ M_\oplus\ \mathrm{yr}^{-1}$. The dashed curve shows a more massive planet with $M = 3\ M_J$, $R = 1.5\ R_J$ accreting at $\dot{M} = 10^{-2}\ M_\oplus\ \mathrm{yr}^{-1}$.

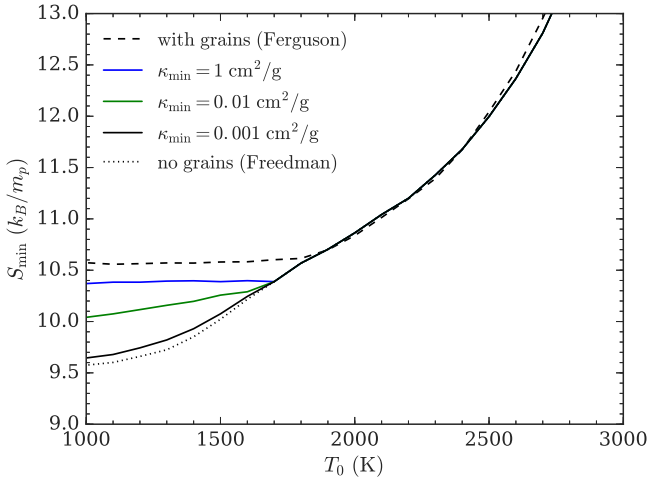

Figure 4. Effect of grain opacity on the minimum entropy $S_{\min}$. The dotted curve is the $\dot{M} = 0.01\ M_\oplus\ \mathrm{yr}^{-1}$ curve from Figure 3. The other curves show the increase of $S_{\min}$ that is due to an increased opacity from grains at low temperatures.

the opacity tables from MESA based on the Ferguson et al. (2005) opacities (specifically the `lowT_fa05_gs98_z2m2_x70.data` table) for $X = 0.7$ and $Z = 0.02$. Second, we model a reduced grain opacity in an approximate way by adding a constant $\kappa_{\min}$ to the dust-free opacity tables from Freedman et al. (2008) for $T < 1700$ K (above approximately this temperature, grains evaporate, e.g., Semenov et al. 2003). A reduction of grain opacity to about 0.3% of the interstellar value (Mordasini et al. 2014a) corresponds to $\kappa_{\min} \sim 10^{-2}\ \mathrm{cm}^2\ \mathrm{g}^{-1}$.

We find that the additional opacity has two effects. The first is to increase the value of $S_{\min}$. This is shown in Figure 4 for $\dot{M} = 10^{-2}\ M_\oplus\ \mathrm{yr}^{-1}$. At temperatures below 1700 K, the additional opacity in the envelope increases the value of $S_{\min}$ by $\approx 0.5\ k_B/m_p$ for $\kappa_{\min} = 10^{-2}\ \mathrm{cm}^2\ \mathrm{g}^{-1}$. This shows that grain opacity can have an effect for accretion onto a planet with an initial value of internal entropy $S_i \lesssim 10.5\ k_B/m_p$. In most of the cases we show below, however, $S_{\min}$ becomes relevant only at higher temperatures where grain opacity is not important.

The second effect is that grain opacity acts to reduce the luminosity of cooling models. For example, a model with the same parameters as in Figure 2 but $T_0 = 500$ K (the lowest temperature available in the Ferguson et al. 2005 tables) and $S_c = 11.0\ k_B/m_p$ has a luminosity at the RCB $L_{\mathrm{RCB}} = 6.9 \times 10^{-4}\ L_\odot$ with molecular opacity alone (opacities of Freedman et al. 2008) and $L_{\mathrm{RCB}} = 6.9 \times 10^{-5}\ L_\odot$ with full grain opacity (opacities of Ferguson et al. 2005). Setting $\kappa_{\min} = 10^{-2}\ \mathrm{cm}^2\ \mathrm{g}^{-1}$ gives $L_{\mathrm{RCB}} = 2.1 \times 10^{-4}\ L_\odot$, which is a few times lower than the grain-free case.

Both of these effects make it harder to produce cold starts. For the rest of the paper we only use the grain-free molecular opacities of Freedman et al. (2008), keeping in mind that dust opacity will act to increase the final entropy in the cooling regime, and so we are being optimistic for the production of cold starts.

3.5. Cooling Timescales During Accretion

Figure 5 shows the cooling luminosity L_{RCB} for a range of model parameters. The different curves show L_{RCB} as a

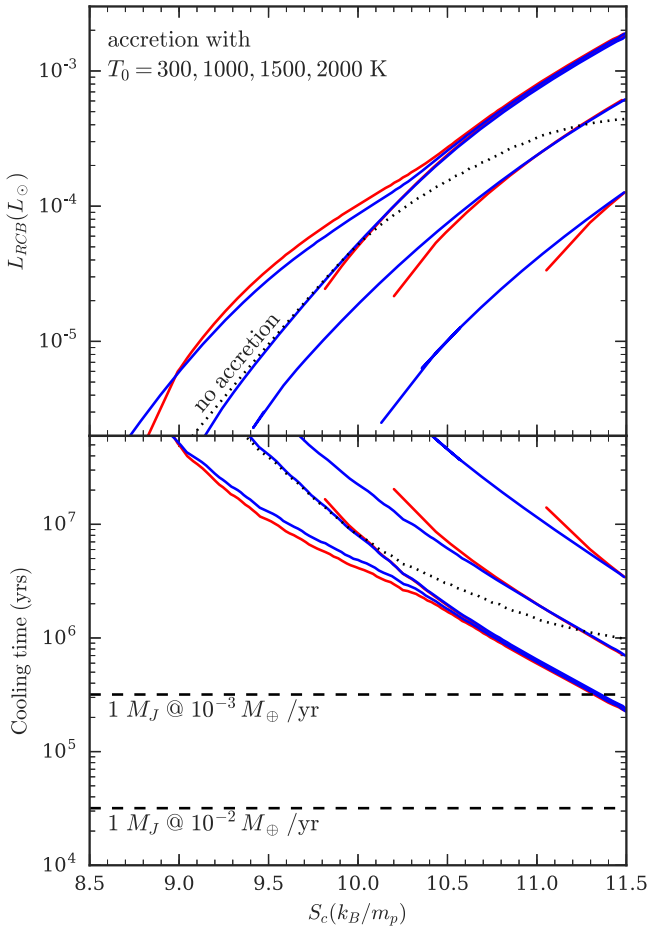

Figure 5. Luminosity at the radiative-convective boundary (upper panel) and cooling timescale (lower panel) as a function of the entropy of the convection zone for accreting models with outer temperatures $T_0 = 300$, 1000, 1500, and 2000 K (from left to right) and $\dot{M} = 10^{-2}\ M_\oplus\ \mathrm{yr}^{-1}$ (red curves) and $10^{-3}\ M_\oplus\ \mathrm{yr}^{-1}$ (blue curves). The dotted curve shows the luminosity and cooling time of an isolated (nonaccreting) planet. The planet mass is $1\ M_J$, and for each value of S_c we set the appropriate radius and the outer boundary pressure to the ram pressure (Equation (3)). The horizontal dashed lines in the lower panel show the time to accrete $1\ M_J$ for each accretion rate.

function of the internal entropy S_c for different boundary temperatures. The dotted curve shows the luminosity of an isolated planet for comparison. The accreting models with $T_0 = 1000$ K and smaller are more luminous than the isolated planets; those with $T_0 = 1500$ or 2000 K are less luminous than an isolated planet.

The models shown are for a specific choice of planet mass, $M = 1\ M_J$, but they can easily be rescaled to other masses. For radiative envelopes, L and M enter the radiative diffusion equation in the combination L/M (see Equation (12); Arras & Bildsten 2006; Marleau & Cumming 2014), and therefore $L_{\rm RCB} \propto M$. We find that this scaling is a good approximation for all our models.

Two different accretion rates are shown in Figure 5. The cooling luminosity $L_{\rm RCB}$ does not depend sensitively on $\dot{M}$. The main effect of changing the accretion rate is to change the minimum value of entropy $S_{\rm min}$ for which we can have a cooling core. Each curve in Figure 5 starts at $S_{\rm min}$ (compare Figure 3). For example, the models with $T_0 = 1000$ K only allow a cooling envelope attached to the interior convection zone for $S_c \gtrsim 9.8\ k_{\rm B}/m_p$ at $\dot{M} > 0.01\ M_\oplus\ {\rm yr}^{-1}$. At lower internal entropies, the planet will accumulate a hot envelope with entropy $\approx 10\ k_{\rm B}/m_p$, which is a potentially much higher entropy than in the convective core.

The lower panel of Figure 5 shows the cooling time of the planet. We calculate the cooling time by taking the cooling time of an isolated gas giant with the same mass and entropy S_c from Marleau & Cumming (2014) and scaling it by the ratio of the RCB luminosity in the accreting envelope to the RCB luminosity without accretion. An outer temperature of 300 K reduces the cooling time by a factor of a few or more; hotter boundaries with $T_0 \gtrsim 1500$ K have longer cooling times than an isolated planet by factors of a few to an order of magnitude.

To reduce the internal entropy substantially during accretion, and therefore make a cold start, the cooling timescale should be shorter than the accretion time. It is striking in Figure 5 that this is almost never the case. Even for a cold outer boundary $\lesssim$1000 K and accretion rate $10^{-3}\ M_\oplus\ {\rm yr}^{-1}$, the cooling time is still comparable to the accretion time. To give a specific example, for an accretion rate of $10^{-2}\ M_\oplus\ {\rm yr}^{-1}$, the accretion time is $\approx 3 \times 10^4$ yr per Jupiter mass. For internal entropy $S_c \gtrsim 11\ k_{\rm B}/m_p$, this is a factor of $\gtrsim$3 times longer than the cooling timescale, which means that while some cooling can occur, we would not expect a large change in entropy during accretion. At $10^{-3}\ M_\oplus\ {\rm yr}^{-1}$, an entropy $11.5\ k_{\rm B}/m_p$ object has a cooling time shorter than the accretion time for $1\ M_J$ and therefore should be able to cool as it forms, but we would not expect it to be very dramatic. For hotter boundaries with $T_0 \gtrsim 1500$ K, the cooling is effectively stalled by the hot envelope.

4. EVOLUTION OF THE PLANET DURING ACCRETION WITH MESA

In Section 3 we studied time-independent snapshots of planetary models. We now use the open-source one-dimensional (1D) stellar evolution code MESA[6] (Paxton et al. 2011, 2013, 2015) to model the time-dependent evolution of a planet during runaway gas accretion. The implementation and evolution of the model[7] is given in Section 4.1. We first adopt a constant temperature T_0 and pressure P_0 at the surface of the planet (Section 4.2) to explore the influence of the entropy $S_0 = S(T_0, P_0)$ of the accreted material on the final state of the planet. We then adopt a more realistic time-dependent outer boundary condition where we set the pressure to the ram pressure and parameterize the outer boundary in terms of the shock temperature T_0 (Section 4.3).

4.1. Details of Planet Model and Simulating Accretion

4.1.1. Starting Model

We create an initial planet model for accretion using the `make_planet` test suite in MESA. We set the mass and radius of the planet, leaving other parameters at their default values, but turning off irradiation. The hydrogen and helium mass fractions are $X = 0.73$, and $Y = 0.25$, respectively, the low-temperature opacity tables are those of Freedman et al. (2008), and the equation of state is given by Saumon et al. (1995). We include a rocky core with mass and radius $10\ M_\oplus$ and $2.8\ R_\oplus$ (i.e., with a mean density of 10 g cm^{-3}), which is implemented in MESA through simple inner boundary conditions for the structure of the modeled planet.

For a given initial mass of the planet, we choose the radius in order to set the desired initial internal entropy. In the core accretion models of Mordasini (2013), the entropy of the planet at the onset of runaway accretion is $\approx 11\ k_{\rm B}/m_p$. To explore the sensitivity to the starting entropy, we consider values of $S_i = 9.5$, 10.45 and 11.6 $k_{\rm B}/m_p$. At these values of entropy, the `make_planet` module has difficulty converging for masses as low as the crossover mass $\lesssim 0.1\ M_J$ because the planet is greatly inflated. To alleviate this problem, we instead start with a higher mass, 0.2, 0.5, and $1\ M_J$ for $S_i = 9.5$, 10.45 and 11.6 $k_{\rm B}/m_p$, respectively.[8] For these three choices of initial mass, we set the radius in `make_planet` to $R = 2$, 5, and $10\ R_J$, which leads to the desired entropy at the onset of accretion.

4.1.2. Accretion and the Outer Boundary Conditions

We now turn on accretion using the `mass_change` control to specify an accretion rate. By default, MESA accretes material with the same thermodynamic properties (i.e., temperature, density, and thus entropy) as the outer layers of the model. This is a useful comparison case that we refer to as thermalized accretion. To model runaway gas accretion, we use the `other_atm` module of the `run_star_extras` file in MESA in order to specify T_0 and P_0. They can be set to constant values for the entire evolution, for example, or be adjusted depending on the state of the planet at any given time (e.g., the mass- and radius-dependent ram pressure given by Equation (3)).

If the deviation from thermalized accretion is too large, MESA may fail to converge and not produce a model. Consequently, if the imposed surface temperature is too high, we slowly increase the temperature from a lower value that does converge to the desired temperature over a timescale on the order of $\sim$1% of the total accretion time to ensure that the final results are not significantly affected. For example, a model accreting at a rate of $10^{-2}\ M_\oplus\ {\rm yr}^{-1}$ with a desired surface temperature of 2500 K will instead begin with 1500 K and

[6] Modules for Experiments in Stellar Astrophysics, version 7623.

[7] Input files for our setup can be found at http://mesastar.org.

[8] We investigated the sensitivity to changing the initial mass and found that the final entropy of the planet changed by $\lesssim 0.3\ k_{\rm B}/m_p$.

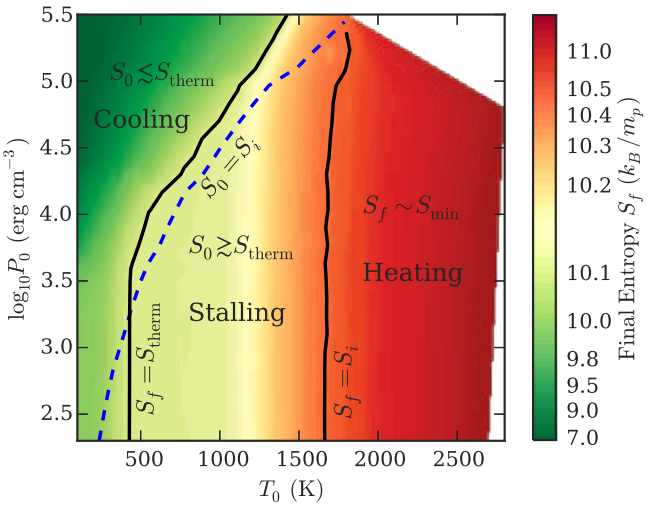

Figure 6. Final entropy (*colorscale*) of a 10 M_J planet accreting at 10^{-2} $M_\oplus$ yr^{-1} as a function of surface temperature T_0 and pressure P_0, held constant. Every model begins with a mass of 0.5 M_J and an initial entropy of $S_i = 10.4$ k_B/m_p. The black line on the right indicates where the final entropy S_f is equal to S_i. The black line on the left indicates where the final entropy is equal to the entropy reached by thermalized accretion $S_{\rm therm} = 10.1$ k_B/m_p. The blue dashed line indicates where the surface entropy S_0 is equal to the initial entropy. The three accretion regimes ("cooling," "stalling," and "heating") are discussed in the text. The colors and contours were obtained by smoothing an appropriately distributed set of 989 independent models.

linearly increase the temperature up to 2500 K over the course of 5000 years.

We do not include any internal heating from planetesimal accretion. Planetesimals can deposit energy deep inside the planet, with maximal luminosity when they penetrate to the rocky core (e.g., see discussion in Section 5.7 of Mordasini et al. 2015). The luminosity is $L_Z = (GM_c/R_c)\dot{M}_Z \approx 10^{-6}\ L_\odot (\dot{M}_Z/10^{-5}\ M_\oplus\ {\rm yr}^{-1})$, where $\dot{M}_Z$ is the accretion rate of planetesimals, and we take a core mass $M_c = 10\ M_\oplus$ and mean core density $\bar{\rho}_c = 5$ g cm^{-3}. Because it is potentially deposited deep inside the convection zone, this luminosity can heat the convection zone from below and cause its entropy to increase. However, the internal luminosities we find are all much greater than L_Z, except for the coldest cases, and we therefore neglect this heat source.

The mesh_delta_coeff parameter controls the length of the grid cells. As a check that the MESA calculations are converging to a physical model, we increase and decrease this parameter by a factor of two, and find no discernible difference in the results. Similarly, we lower the `varcontrol_target` parameter by an order of magnitude. This parameter controls the size of the time step. Again, we find no difference.

4.2. Identification of Accretion Regimes

We first survey the final entropies obtained by holding T_0 and P_0 fixed during accretion. We construct a grid of models with T_0 and P_0 ranging from 100 to 2700 K and $10^{2.3}$ to $10^{5.5}$ erg cm^{-3}, respectively. For these values the surface entropy S_0 ranges from $\approx$6 to 20 k_B/m_p (Appendix A). In this section, we use an accretion rate of 10^{-2} $M_\oplus$ yr^{-1}, an initial mass of 0.5 M_J, and an entropy of 10.45 k_B/m_p.

The results of this survey are shown in Figure 6. We find that the final entropies can be separated into three different regimes. The black line on the right shows where the final entropy of the planet at the end of accretion is equal to the initial entropy. In the region to the right of this line, the final entropy is greater than the initial entropy, hence the "heating" regime. In the region to the left of this line, the final entropy is lower than the initial entropy, and this can be further subdivided into two more regions.

The black line in the left part of Figure 6 shows where the final entropy of the planet is equal to the value it would reach under thermalized accretion, in which the accreted material has the same thermodynamic properties as the planet. In a sense, this scenario allows the planet to cool while increasing its mass. The final entropy reached under this conditions is referred to as $S_{\rm therm}$. In most cases, if $S_0 > S_{\rm therm}$, then the final entropy of the planet will be between S_i and $S_{\rm therm}$ in the "stalling" regime, since the planet has not cooled as much as it could have. To the left of the leftmost black line, we have the region where $S_f < S_{\rm therm}$, which is again characterized by having $S_i < S_{\rm therm}$. In this "cooling" regime, the planet cools by a greater amount than it would have and thus ends up at a lower final entropy.

In Figure 7 we show the internal profiles for planets accreting in each regime at different points throughout their accretion, in order to understand what drives their evolution. The top panel shows the evolution under "cooling" accretion conditions, where the surface entropy is at a value of $S_0 \approx 8.7$ k_B/m_p, which is below $S_{\rm therm} = 10.1$ k_B/m_p. The internal entropy decreases rapidly, such that it drops to almost the surface entropy S_0 after accretion of about one Jupiter mass or about 30,000 years. This corresponds to the cold-outer-boundary envelope discussed in Section 2. The internal entropy structure is such that the entire planet is convective as it cools down.

The middle panel of Figure 7 shows the stalling regime, in which the surface entropy is higher than $S_{\rm therm}$, but still low enough to smoothly attach to the interior of the model (Section 3.2). A radiative region forms in the outer layers, which pushes the RCB to higher pressures and reduces the luminosity of the convective core (Section 3.5). The internal entropy still decreases, but at a slower rate than in the cooling scenario or thermalized accretion.

The bottom panel of Figure 7 shows the heating regime, in which the difference in entropy between the surface and interior is too large for the envelope to accommodate, as discussed in Section 3.3. In this case, the accreted material accumulates to form a second convection zone above the original convective core. We note that a temperature inversion is associated with the jump between the original low convective entropy zone and the new higher entropy convection zone; a similar temperature inversion was seen for strongly irradiated hot Jupiters by Wu & Lithwick (2013). The conduction timescale in the planet interior is very long, so that the temperature inversion remains at the same mass coordinate as accretion proceeds. As mentioned in Section 4.1.2, the surface temperature is increased linearly from 1500 to 2400 K over the course of 5000 years to help convergence. This gives an initial rise of the surface entropy for $M \lesssim 0.7\ M_J$.

To show how the boundary conditions determine the post-accretion planet properties, Figure 8 shows the final interior entropy S_f as a function of the surface entropy S_0 for a final planet mass of 10 M_J. In the hot models that develop two internal convection zones, we choose the higher internal entropy value since most of the mass of the planet is at this higher entropy value. This in turn is due to the upper zone appearing sufficiently early in the accretion history; for

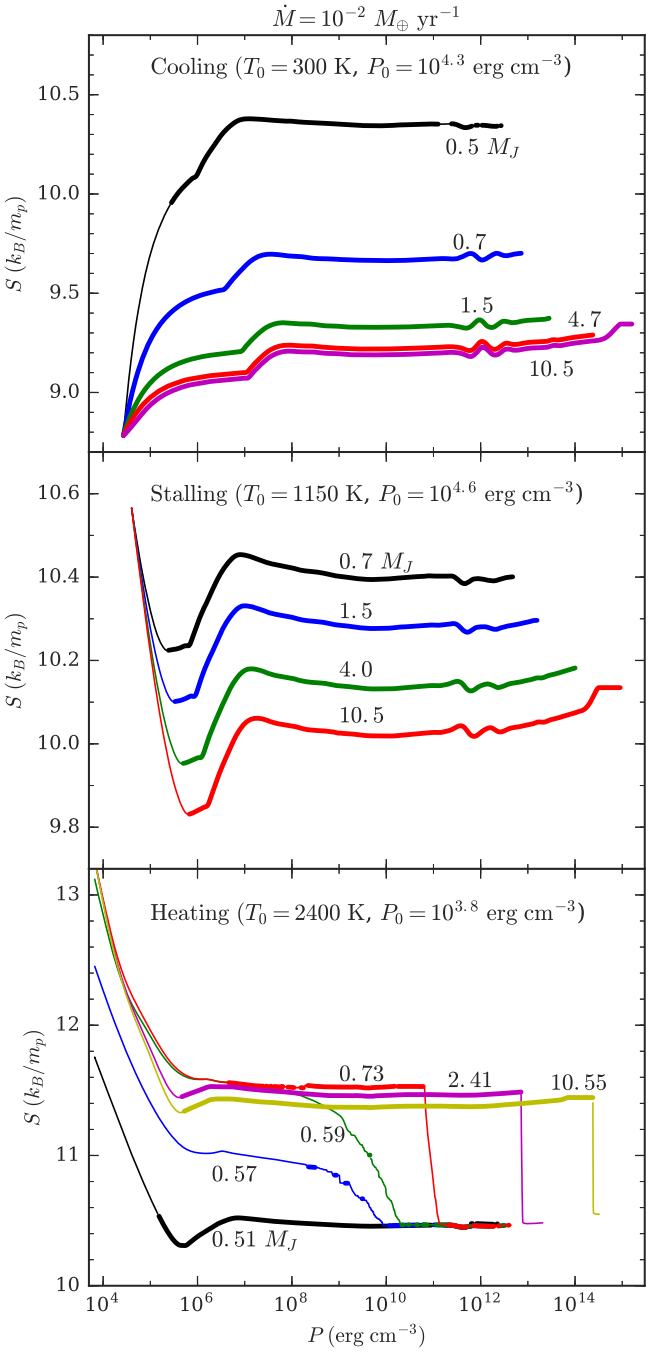

Figure 7. Internal entropy profiles for a planet with initial entropy $S_i = 10.45\ k_B/m_p$ undergoing accretion with boundary conditions (T_0 and P_0). They are chosen to correspond to the three accretion regimes identified in Figure 6 (see panel titles), with entropies for the accreted material of $S_0 = 8.7$, 10.6, and 13 k_B/m_p, respectively (top to bottom panel). The total mass (labels next to curves) is used to track the time evolution of the models from 0.5 to 10.5 M_J. Convective regions in the profiles, according to the Schwarzschild criterion, are shown by thick lines. Note that each panel uses a different scale on the vertical axis.

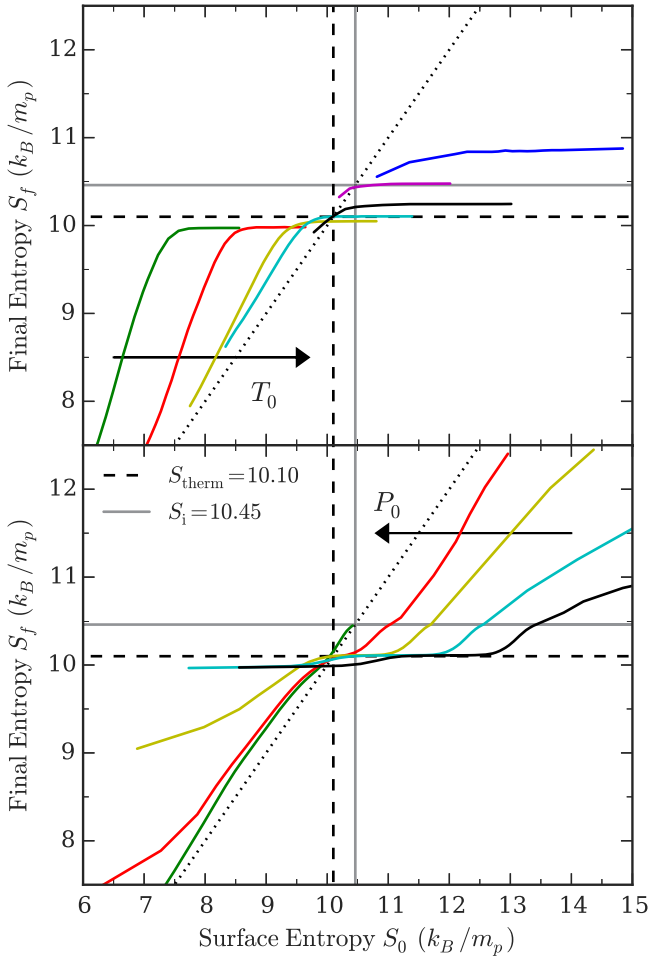

Figure 8. Top panel: final internal entropy of the planet as a function of the entropy of the accreted surface material. The models are the same as in Figures 6 and 7. For structures with two convective zones, the entropy of the upper zone is used, as discussed in the text. The colored lines correspond to constant values of the shock temperature T_0 = 100, 150, 300, 450, 1350, 1750, and 2100 K (bottom left to top right). Along each constant-T_0 curve, the surface pressure P_0 decreases from left to right. We also display the value of the initial entropy of the model ($S_i = 10.46\ k_B/m_p$; solid gray line) and the final entropy reached with thermalized accretion ($S_{\mathrm{therm}} = 10.10\ k_B/m_p$; dashed black line). The diagonal dotted line shows where the final and surface entropy are equal. Bottom panel: same results as in the top panel, but plotted as curves of constant shock pressure P_0 for $\log_{10}(P_0/\mathrm{erg\ cm}^{-3}) = 2.3$, 3.2, 4.1, 4.8, and 5.5 (top right to bottom left); along each curve, the shock temperature T_0 increases from left to right.

instance, in Figure 7, only the inner $\approx 0.5\ M_J$ are frozen in at $S \approx S_i = 10.45\ k_B/m_p$.

Models with $S_0 < S_{\mathrm{therm}}$ (to the left of the dashed vertical line in Figure 8) are in the cooling regime. They show that the amount of cooling at a given value of surface entropy S_0 depends on the explicit choice of P_0 and T_0. Moreover, in this regime the dependence on pressure is stronger than the dependence on temperature. For a fixed surface entropy, moving the surface to higher pressure means that the entropy must increase at a faster rate to match the internal value, implying a higher value of $\nabla - \nabla_{\mathrm{ad}} \propto dS/dP$ and therefore a higher convective luminosity (Equation (13)). A higher surface pressure therefore gives more rapid cooling, resulting in a lower value of S_f at the end of accretion. It should be noted that cooling below 9 k_B/m_p requires high pressures ($P_0 > 10^{4.2}$ erg cm^{-3}) and low temperatures ($T_0 < 450$ K).

For $S_0 > S_{\mathrm{therm}}$, we show the stalling and heating regimes. In the heating regime, the final entropy lies above the initial entropy and increases with T_0, with almost no dependence on P_0. In the stalling regime, the final entropy lies between the initial value S_i and S_{therm}. As T_0 increases in the stalling regime, the RCB is pushed to higher pressure, reducing the luminosity at the RCB and delaying the cooling further so that the final

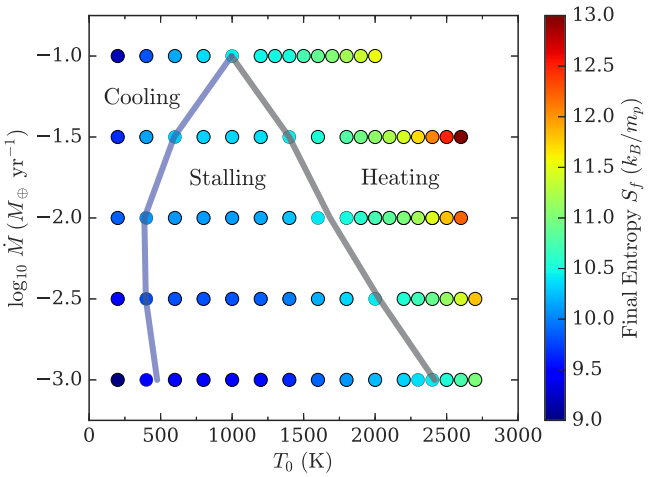

Figure 9. Final internal entropy (*colorscale*) of the planet as a function of shock temperature T_0 and accretion rate $\dot{M}$. The solid black line indicates the initial entropy of the models (here $S_i = 10.45\ k_B/m_p$), thus delineating the stalling and heating regimes. The solid blue line indicates the final internal entropy reached under thermalized accretion, separating the cooling and stalling regimes. This value depends on the accretion rate, so that the entropy value changes along the blue line.

entropy of the planet is approximately equal to the initial entropy S_i. This is a similar effect to the delayed cooling of irradiated or Ohmically heated hot Jupiters (e.g., Arras & Bildsten 2006; Huang & Cumming 2012; Wu & Lithwick 2013). In this regime, the degree of cooling is insensitive to P_0 because the envelope is close to isothermal (e.g., see Figure 2), so that the temperature of the envelope set by T_0 determines the RCB location.

Additionally, the same grid of T_0 and P_0 was run for an initial entropy $S_i = 11.5\ k_B/m_p$. The final entropy reached under thermalized accretion was essentially the same, since for high initial entropies this value will be set by the amount of time available to cool. Since the heating/stalling boundary is located at the initial entropy, this only increased the "height" of the stalling regime, i.e., the distance between the horizontal lines in Figure 8.

4.3. The Outcome of Runaway Accretion

In order to model runaway accretion, we now use the ram pressure $P_{\rm accr}$, given by Equation (3), as the outer boundary pressure P_0. The ram pressure evolves with time as the mass and radius of the planet change. We hold the outer temperature T_0 constant. In reality, the shock temperature will also depend on mass and radius and change with time (e.g., as in Equation (2)), but without a specific model, we leave it as a constant parameter describing the post-shock conditions (Section 5).

Figure 9 shows the final central entropy of the planet as a function of T_0 and $\dot{M}$, having started with entropy $S_i = 10.45\ k_B/m_p$. We again see the separation into three accretion regimes. The blue line is drawn such that the entropy along it is at the value that would be reached by thermalized accretion at each accretion rate. The entropies to the left of the blue line are lower, indicating the cooling regime. The black line is drawn such that the entropy along it is equal to the initial entropy. The entropy to the right of the black line is greater, indicating the heating regime. Between the blue and black lines, where the entropy lies between the initial value and the value reached by thermalized accretion, is the stalling regime.

In the cooling regime, the entropy reaches a minimum of $\sim 9\ k_B/m_p$, whereas we found much lower values in Section 4.2. The difference arises because the ram pressure never becomes high enough to significantly decrease the surface entropy. For example, with $\dot{M} = 10^{-2}\ M_\oplus\ \mathrm{yr}^{-1}$, a final radius $R \approx 1\ R_J$, and mass $M = 10\ M_J$, the ram pressure is always $P_{\rm accr} \lesssim 10^4\ \mathrm{erg\ cm}^{-3}$ since $P_{\rm accr} \propto M^{1/2}R^{-5/2}$ (Equation (3)); when we compare this to Figure 8, we see that this does not lead to significant cooling.

The internal entropy in the cooling regime depends in a non-monotonic way on the accretion rate. When we increase the accretion rate from 10^{-2} to $10^{-1}\ M_\oplus\ \mathrm{yr}^{-1}$, we obtain a lower entropy because the ram pressure is higher for a higher accretion rate, leading to a higher luminosity (Figure 8). At lower accretion rates $\dot{M} \gtrsim 10^{-3}\ M_\oplus\ \mathrm{yr}^{-1}$, the luminosity is lower than at $\dot{M} \gtrsim 10^{-2}\ M_\oplus\ \mathrm{yr}^{-1}$, but the accretion timescale is much longer so that more cooling can occur and the final entropy decreases with decreasing $\dot{M}$. For $\dot{M} \gtrsim 10^{-2}\ M_\oplus\ \mathrm{yr}^{-1}$, the boundary between the cooling and stalling regimes occurs at higher temperature for a higher accretion rate. The reason is that the ram pressure is higher, and a higher temperature is needed to achieve an entropy that is high enough to be in the stalling regime. For $\dot{M} \lesssim 10^{-2}\ M_\oplus\ \mathrm{yr}^{-1}$, the boundary temperature is almost independent of accretion rate because the boundary moves to low pressure (horizontal parts of the curves in the top panel of Figure 8).

In the stalling regime, the final entropy increases with accretion rate because there is less time available to cool, and it increases with temperature because a hotter envelope reduces the cooling luminosity. In the heating regime, the final entropy is set by $S_{\rm min}$, which increases with temperature and accretion rate. The values of entropy agree well with the values of $S_{\rm min}$ calculated in the envelope models (Figure 3). The boundary between the stalling and heating regimes can be understood by finding the temperature for which $S_{\rm min} \approx S_i$ at each $\dot{M}$.

Figure 10 shows the dependence of the internal entropy on planet mass for different values of S_i, $\dot{M}$, and T_0, i.e., the post-formation, initial entropy ("initial" in terms of the pure cooling phase; e.g., Marley et al. 2007). In each panel, the blue dot shows the initial mass and entropy. For the cooling cases, the curves rapidly drop with increasing mass at first, but then flatten at higher masses. Most of the cooling occurs by the time that they have reached $\approx 4\ M_J$ (as is also shown by the entropy profiles in Figure 7). The models in the heating regime show a final entropy that only slightly depends on total mass ($\Delta S \approx 0.2\ k_B/m_p$ from 1 to 10 M_J at a given T_0). In these cases, the hot envelope deposits matter with entropy $S_{\rm min}$ in a second convection zone immediately after accretion starts, as described in the Section 4.2. However, Figure 3 shows that $S_{\rm min}$ decreases with planet mass, so that the planet very quickly enters the stalling regime where the accreting envelope smoothly joins the high-entropy outer convection zone. This causes the internal entropy to decrease slightly with planet mass after the initial rise. This result differs from the hot-start accretion models of Mordasini (2013), which show an increasing entropy with mass and thus yield a tuning-fork shape with the cold starts.

A higher initial entropy acts to shift the final entropy upwards. If the shift is large enough, it can push a model that was once in the stalling regime into the cooling regime. An example of this is

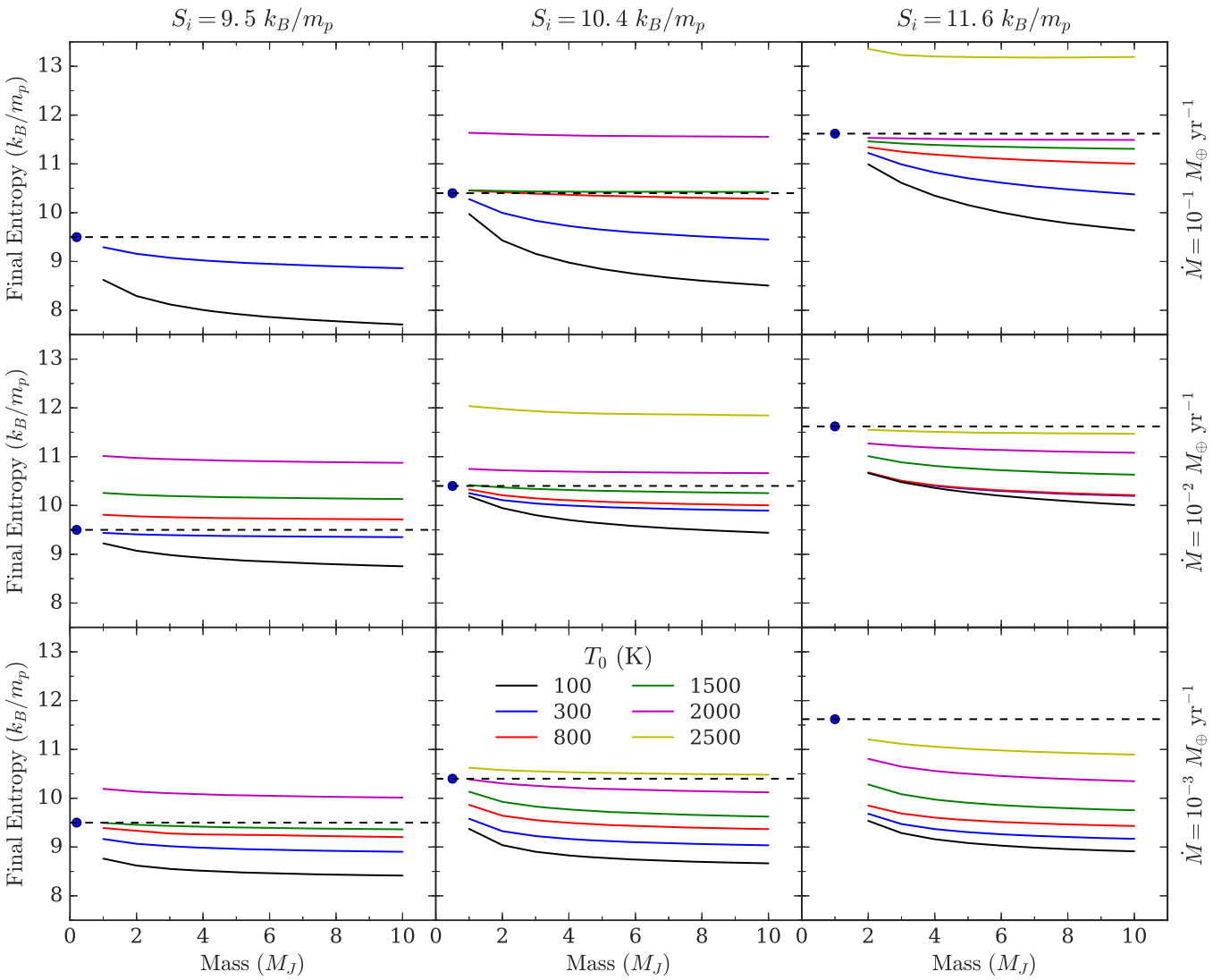

Figure 10. Final entropy as a function of mass for accretion models. Each panel shows a particular choice of $\dot{M}$ and S_i indicated by the labels along the top and right of the figure. The blue dots and dashed lines indicate the initial entropy and mass, which are (9.5, 0.2), (10.4, 0.5), and (11.6, 1.0) (k_B/m_p, M_J), from the left column to the right column. The lines correspond to accretion with different surface temperature T_0 (see legend). Not all temperatures are shown in some panels because of convergence issues at lower values of S_i and higher values of $\dot{M}$ or T_0.

the case of $\dot{M} = 10^{-3}\ M_\oplus\ \mathrm{yr}^{-1}$ and $T_0 = 2000$ K, which is in the stalling regime for $S_i = 9.5\ k_B/m_p$ and in the cooling regime for $S_i = 11.5\ k_B/m_p$.

5. SUMMARY AND DISCUSSION

In this paper, we investigated the fate of newly accreted matter during the runaway accretion phase of gas giant formation. Since most of the mass of the planet is added during this phase, it is crucial for determining the luminosity of the planet once it reaches its final mass.

5.1. The Accretion Process

We showed that solutions for the envelope of an accreting planet take three different forms (Sections 3.2 and 3.3), which leads to three different accretion regimes (Section 4.2 and Figure 7). Figure 6 shows the final outcome of accretion: the internal entropy of the planet resulting from accretion with different choices of outer boundary temperature and pressure T_0 and P_0. The accretion regime depends on the difference between the entropy of the material deposited by the accretion shock $S_0(T_0, P_0)$ and the initial internal entropy S_i:

1. The *cooling regime*. For $S_0 \lesssim S_i$, the planet becomes fully convective, and the superadiabatic gradient drives a high luminosity that leads to rapid cooling. The cooling luminosity is sensitive to the boundary pressure P_0, with higher P_0 leading to faster cooling. When the cooling is rapid enough compared to the accretion timescale, the end state of this regime is that the internal entropy becomes equal to the surface entropy $S_f \approx S_0$. This regime occurs for low boundary temperatures $T_0 \lesssim$ 500–1000 K.
2. The *stalling regime*. For $S_0 \gtrsim S_i$, the entropy decreases inwards in a radiative envelope. Provided the entropy contrast is not too great, the envelope smoothly joins the interior convection zone. The hot envelope causes the RCB to lie at higher pressure than in an isolated cooling planet with the same internal entropy, lowering the luminosity at the RCB and slowing the cooling. In this regime, the final entropy lies close to the initial value of entropy at the onset of accretion $S_f \lesssim S_i$, depending on

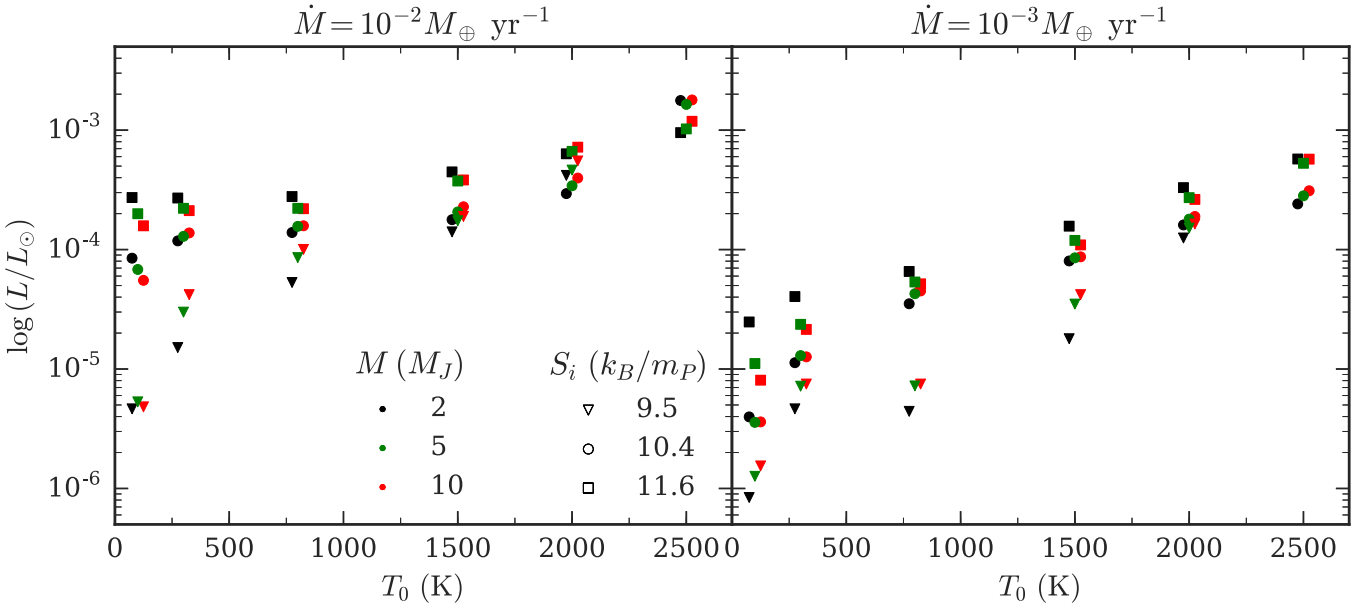

Figure 11. Luminosity at the onset of post-accretion cooling as a function of surface temperature during accretion for $\dot{M} = 10^{-2}\ M_\oplus$ yr^{-1} (*left panel*) or $\dot{M} = 10^{-3}\ M_\oplus$ yr^{-1} (*right panel*). The colors indicate the final planet mass, while the different symbols indicate the initial entropy of the object at the beginning of accretion (see the legend). For visual clarity, the markers are given a temperature offset of −25, 0, and +25 K for a respective final mass of 2, 5, and 10 M_J.

how much the cooling is slowed. This regime occurs at intermediate temperatures $T_0 \approx$ 1000–2000 K.

3. The *heating regime*. For boundary temperatures $T_0 \gtrsim$ 2000 K, the entropy difference $\Delta S = S_0 - S_i$ cannot be accommodated by the radiative envelope. Instead, the entropy decreases inwards through the envelope to a value $S_{\rm min} > S_i$ (Section 3.3, Appendix B, Figure 3), and a second convection zone with entropy $S_{\rm min}$ accumulates on top of the original convective core. Because the minimal entropy $S_{\rm min}$ decreases with increasing planet mass, the envelope quickly moves into the stalling regime as the planet mass increases, and the planet accumulates most of its mass with entropy close to the original $S_{\rm min}$.

Our results show that the luminosity of a young gas giant formed by core accretion depends not only on the outer boundary conditions (e.g., the shock temperature T_0) and accretion rate, but also on the initial entropy S_i when runaway accretion begins, since it determines whether accretion occurs in the cooling, stalling, or heating regimes. The thermal state of the young planet therefore in principle provides a link to the structure of the accreting core soon after the crossover mass is reached. This point was also made by Mordasini (2013), who found that the final entropy sensitively depended on the core mass because it sets the entropy of the envelope at detachment. We showed here that the final entropy is close to the entropy at the start of runaway accretion for a wide range of intermediate temperatures for which accretion is in the stalling regime ($T_0 \approx$ 1000–2000 K, see Figure 9).

5.2. Cold or Hot Starts?

The luminosity of the planet after formation L_p is shown in Figure 11. We calculate this luminosity by taking the internal entropy at the end of accretion (for the hot cases, this is the entropy in the hotter, outer convection zone) and constructing a new planet with the same mass and internal entropy in MESA. This avoids convergence issues that arise when changing from accreting to cooling surface boundary conditions at the end of accretion.

Figure 11 shows that cold starts require that we choose the lowest values of boundary temperature $T_0 < 300$ K (comparable to typical nebula temperatures $T_{\rm neb}$), accretion rate $\dot{M} = 10^{-3}\ M_\oplus$ yr^{-1}, and initial entropy $S_i = 9.5\ k_{\rm B}/m_p$. In these cases, we find luminosities that are comparable to and even lower than the cold-start luminosities of Marley et al. (2007), who found 2–3 $\times\ 10^{-6}\ L_\odot$ for $M =$ 4–10 M_J and $\approx 6 \times 10^{-6}\ L_\odot$ for $M = 2\ M_J$. However, increasing any of these parameters beyond these lowest values gives higher luminosities than Marley et al. (2007). For example, $\dot{M} = 10^{-2}\ M_\oplus$ yr^{-1} (the limiting accretion rate assumed by Marley et al. 2007) gives $L_p \gtrsim 5 \times 10^{-6}\ L_\odot$, even for $T_0 = 100$ K. Increasing T_0 beyond 300 K gives $L_p \gtrsim 5 \times 10^{-6}\ L_\odot$ even for $\dot{M} = 10^{-3}\ M_\oplus$ yr^{-1}.

Temperatures as low as $T_0 \sim T_{\rm neb}$ are possible within the boundary prescription of Bodenheimer et al. (2000) when the flow remains optically thin throughout the growth of the planet. However, the situation in the literature regarding the outer boundary conditions for cold accretion is somewhat confused. The boundary conditions often used in energy approaches to cold accretion, namely that $L \approx 4\pi R^2 \sigma T_{\rm eff}^4$ and $P_0 = (2/3)(g/\kappa)$ (e.g., Hartmann et al. 1997; Mordasini 2013, see Section 2.1), where $T_{\rm eff}$ is the effective temperature, i.e., the usual boundary conditions for a cooling planet, give temperatures significantly higher than $T_{\rm neb}$. In our models these conditions do not lead to cold starts. The cooling time of the planet is generally longer than the accretion timescale (lower panel of Figure 5), so that this cooling boundary condition leads to only a small change in entropy during accretion (see the difference between the horizontal solid and dashed lines in Figure 8). Only by holding the boundary temperature to a low value are we able to drive a luminosity that is high enough to accelerate the cooling and signficantly reduce the internal entropy on the accretion timescale.

However, as discussed in Section 2.1, shock models that have been developed in the context of star formation (Stahler

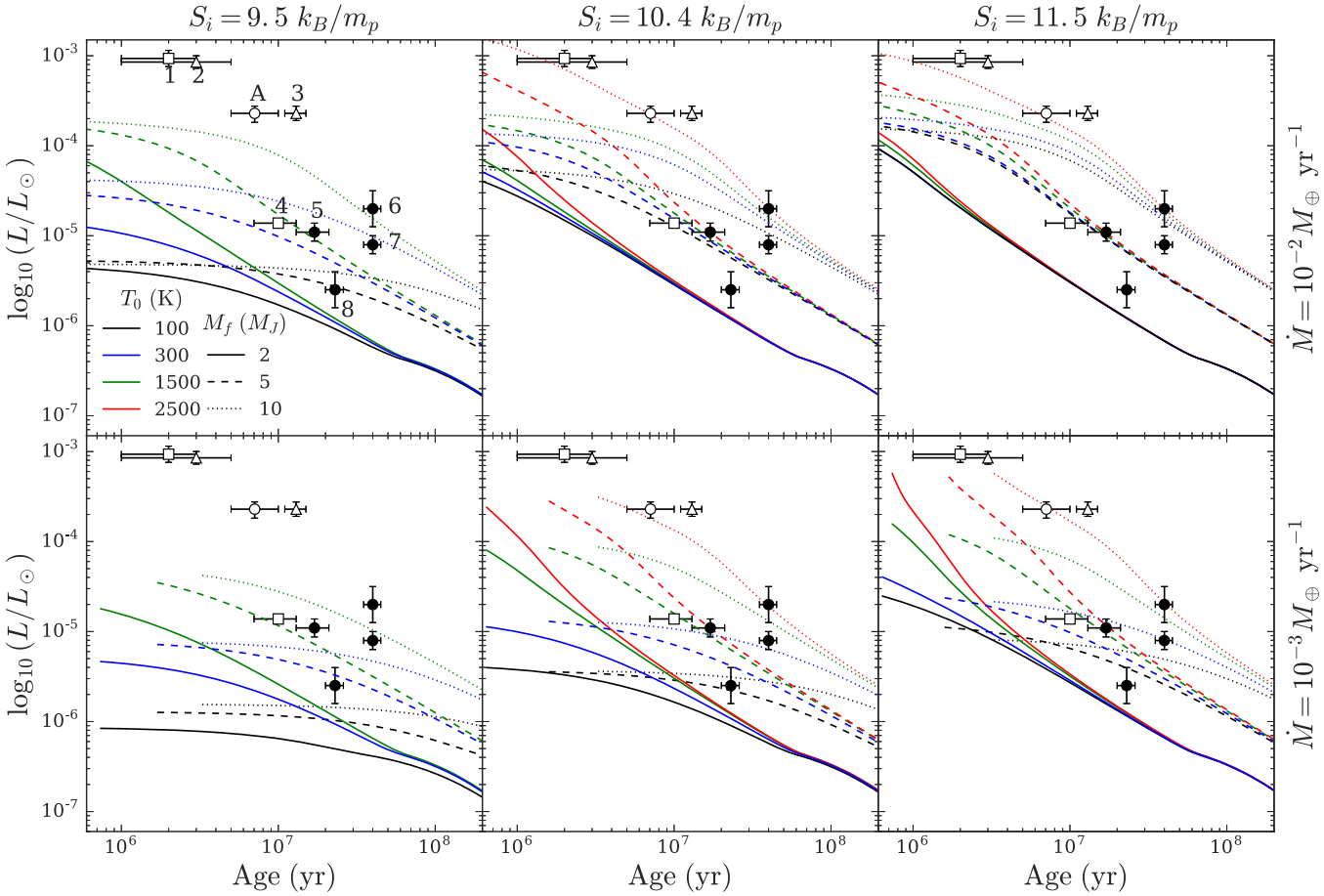

Figure 12. Post-accretion cooling compared with directly imaged exoplanets. The curves show the evolution of the luminosity after accretion is completed for final masses $M_f = 2$, 5, and 10 M_J in MESA (line style) and surface temperature during accretion $T_0 = 100$–2500 K (line color). The entropy at the beginning of accretion (the accretion rate) is constant along columns (rows); see top (right) titles. Because these are post-accretion luminosities, the curves begin at different ages based on the total accretion time, which depends on $\dot{M}$ and the final mass. The data points are for objects with hot-start mass $\lesssim$10 M_J from the compilation of Bowler (2016) as well as the protoplanet HD 100546 b, and use the age of the host star: 1: ROXs 42B b (Currie et al. 2014a), 2: 2M0441+2301B b (Todorov et al. 2014), 3: HD 106906 b (Bailey et al. 2014), 4: 2M1207 3932 b (Chauvin 2004), 5: HD 95086 b (Rameau et al. 2013), 6: HR 8799 d (Marois (2008)), 7: HR 8799 b (Marois (2008)), 8: 51 Eri b (Macintosh et al. 2015), A: HD100546 b (Quanz 2015). The symbol type indicates objects around brown dwarfs (open squares), objects at >100 au (open triangles), planets at <100 au orbiting stars (closed circles), and protoplanets (open circle).

et al. 1980; Commerçon et al. 2011) and planet accretion (Marleau et al. 2016) suggest that the surface temperature is likely to be significantly higher than either of these prescriptions for cold starts. In these models, the gas at the surface of the planet is heated by some fraction of the accretion luminosity that is generated at the shock to a temperature $T_{\rm hot}$ given by $4\pi R^2 \sigma T_{\rm hot}^4 \sim L_{\rm accr} \approx GM\dot{M}/R$. In that case, our results suggest that core accretion will result in hot starts, with high entropy $S_c \sim 12\ k_{\rm B}/m_p$ set by $S_{\rm min}$ (Section 3.3) and luminosity $L_p \gtrsim 10^{-4}\ L_\odot$. The planet grows by accumulating hot material on the outside of the original convective core. The entropy $S_{\rm min}$ depends on the accretion rate, but will be difficult to constrain from observed luminosities given the initial rapid cooling for hot starts.

5.3. Comparison to Data

The subsequent cooling of the planets is shown in Figure 12 and is compared to measured luminosities of directly imaged planets. We include those planetary-mass companions listed in Table 1 of Bowler (2016) that are consistent with a hot-start mass $\lesssim$10 M_J (the maximum mass in our models) with ages $\lesssim 10^8$ years, as well as the protoplanet HD 100546 b, which has a bolometric luminosity given by Quanz (2015). The four points numbered 5–8 refer to planetary companions orbiting at <100 au, and so are perhaps most likely to have formed by core accretion. The cooling curves depend on both S_i and T_0 (which set the post-formation entropy) and the planet mass, so that determining the formation conditions is difficult without an independent measurement of the planet mass (e.g., Marleau & Cumming 2014). Even then, Figure 12 shows that at the age of these planets (≈20–40 Myr), the variation in luminosity with shock temperature T_0 is less than a factor of a few and can be much smaller for low planet masses and hotter initial conditions. Younger planets (with ages $\sim 10^6$–10^7 years) have a better memory of their post-formation state. However, of the other low-mass objects shown, 2M 0441 b and 2M 1207 b orbit brown dwarfs, and ROXs 42Bb and HD 106906 are both seen at wide separations (140 and 650 au, respectively), therefore it is not clear whether they formed by core accretion.

The remaining data point is HD 100546 b, which is thought to be a protoplanet that is currently undergoing accretion from the circumstellar disk. The evidence of core accretion, along with its younger age of $\sim 5 \times 10^6$ years, places it in the range of planets that will be the most useful in understanding the properties of planets produced by core accretion. Additionally,

as previously mentioned in Section 1, it appears that the intrinsic luminosity of the planet can be distinguished from the accretion luminosity, which is an important point to consider when discussing accreting objects. Figures 11 and 12 show that a luminosity of $>10^{-4}\ L_{\odot}$ is obtained in our models only for hot outer boundaries $T_0 \gtrsim 2000$ K or higher entropies at the onset of runaway accretion $S_i \gtrsim 10\ k_B/m_p$.

Of all the objects mentioned above, the requirement to tune parameters to low values to achieve a cold start has the greatest implications for 51 Eri b, which, with a bolometric luminosity of 1.6–4 $\times\ 10^{-6}\ L_{\odot}$ (Macintosh et al. 2015), is perhaps the most likely observed candidate for a cold start. Figure 12 shows that the mass of 51 Eri b could be 10 M_J if $T_0 = 100$ K, but even a small increase to $T_0 = 300$ K requires a lower mass $M \lesssim 3\ M_J$. Therefore it seems likely that the mass of 51 Eri b is close to the hot-start mass, unless the shock temperature can be maintained close to $T_{\rm neb}$ throughout accretion.

5.4. Future Work

Our results were obtained holding T_0 and $\dot{M}$ constant during accretion, as the focus of this work was a parameter space study of the effect of particular boundary conditions on the formation of the planet. However, considering a more complex (and realistic) accretion history with time-dependent boundary conditions could result in a different dependence on final mass. For example, the hot-start models produced in our hot accretion regime have a final internal entropy that is relatively independent of planet mass. This differs from the hot-accretion models of Mordasini (2013), which show increasing entropy as the planet grows in mass, as in the standard hot-start branch of the tuning-fork diagram (e.g., compare Figure 2 of Mordasini 2013 with Figure 2 of Marley et al. 2007). Indeed, preliminary work in which we use a surface temperature that depends on the accretion luminosity (as in Stahler et al. 1980) shows agreement with traditional tuning-fork diagrams for hot starts, i.e., an increasing entropy with final mass.

An additional point related to the consequences of a non-constant surface temperature concerns Section 4.2, where we showed that for heating models an outer convective zone made up of the hotter accreted material forms above the initial, lower-entropy core. In the case of constant T_0, the planet immediately enters the heating regime, so that at the end of accretion the higher entropy zone constitutes a large percentage of the mass (95% in our 10-M_J models). However, when T_0 is set to the time-dependent $T_{\rm hot}$, it increases with time, and with it, the entropy of the accreted material. Therefore, the final internal structure of the planet is different from what is currently seen. This has bearings on the cooling of the object if, for example, an inner radiative region forms (Leconte & Chabrier 2012), but the extent of this effect is currently unclear. A possibility is that thermally irregular internal structures lead to differences even between hot-start cooling curves, implying further uncertainties when estimating the masses of such planets.

One of the other goals of this work has been to develop MESA as a tool for studying planet formation; we make our `inlist` and `run_star_extras` files available at http://mesastar.org. It would be interesting to explore further modeling of gas giant formation in MESA, and overcome some of the limitations of our models. This will require taking energy deposition by planetesimals into account (see review in Section 5.7 of Mordasini et al. 2015), modeling the contribution of dust grains to the envelope opacity (e.g., Mordasini 2014b; Ormel 2014), including possible composition effects on convection (e.g., Nettelmann et al. 2015), and extending to lower masses than considered here (see Chen & Rogers 2017).

5.5. Concluding Remarks

We have focused on the runaway accretion phase of gas giant formation and its role in determining the luminosity of young gas giant planets. The results highlight the importance of understanding the physical factors that set the entropy of the planetary embryo while it is still attached to the nebula, and the temperature of the post-shock gas during runaway accretion. This in particular calls for further investigation of the physics occurring directly at the accretion shock, as in Marleau et al. (2016). Depending on the shock temperature, the post-formation luminosity spans the full range from cold-start to hot-start models. This further emphasizes the point made by Mordasini (2013) that high luminosities need not be associated exclusively with formation by gravitational collapse. Beyond the standard core-accretion models, accretion is possibly not spherically symmetric (Lovelace et al. 2011; Owen & Menou 2016; Szulágyi & Mordasini 2016), which also needs to be taken into account.

We conclude with a few comments pertaining to observations. Obtaining spectroscopy of young forming objects could significantly help to separate the contribution of the shock (also as traced by H α as for the LkCa 15 system; Sallum et al. 2015) from that of the photosphere. The latter is likely similar to a (very-) low-gravity L/M brown dwarf because of the large radius and high surface temperature of the protoplanet (see Equation (2)). Moreover, determining the mass by radial velocity or astrometry, or deriving constraints on it from the morphology of the disk (Bowler 2016), would enable breaking the degeneracy between hot and cold starts (Marleau & Cumming 2014). Finally, once mass information is available for a sufficient number of directly imaged planets, it might be feasible to statistically constrain parameters such as the entropy at the beginning of accretion, for instance, in the framework of population synthesis (Mordasini et al. 2012). Thus, exploiting direct-imaging observations by combining them to studies of all factors that set the post-formation thermal state will help constrain the formation mechanism of gas giants.

The authors would like to thank the referee for comments and insights that helped clarify and improve this paper. D.B. acknowledges support from a McGill Space Institute (MSI) fellowship as well as a scholarship from the Fonds de Recherche Québécois sur la Nature et les Technologies (FQRNT). Additional thanks are given to the participants of the MESA 2016 summer school. A.C. is supported by an NSERC Discovery grant and is a member of the Centre de Recherche en Astrophysique du Québec (CRAQ). G.D.M. was supported in part by a fellowship of the FQRNT and acknowledges support from the Swiss National Science Foundation under grant BSSGI0_155816 "PlanetsInTime." Parts of this work have been carried out within the frame of the National Centre for Competence in Research PlanetS supported by the SNSF.

APPENDIX A
THE ENTROPY IN THE ENVELOPE

It is a good approximation in the envelope of the planet to assume an ideal gas consisting of molecular and atomic hydrogen as well as helium, in which case we can derive a simple formula for the entropy as a function of pressure and temperature. The ideal gas equation of state is $P = \rho k_B T/\mu m_p$ where the mean molecular weight μ is given by

$$\mu^{-1} = \frac{1 - Y}{1 + \chi_{H_2}} + \frac{Y}{4},$$

the molecular fraction $\chi_{H_2} = n_{H_2}/(n_{H_2} + n_H)$ (i.e., χ_{H_2}=1 (0) is purely molecular (atomic) hydrogen), and Y is the helium mass fraction. The number densities of H and H_2 can be computed from the Saha equation

$$\frac{n_{H_2}}{(n_H)^2} = \frac{n_{Q,H_2} z_r}{(n_{Q,H})^2} e^{\Delta\epsilon/k_B T}, \tag{18}$$

where $n_{Q,i} = (2\pi\mu_i m_p k_B T)^{3/2}/h^3$ and $m_p\mu_i$ is the mass of species i. We also consider that for hydrogen gas $n_{H_2} + n_H = P/k_B T$. The ionization energy $\Delta\epsilon$ is 4.48 eV = 7.24×10^{-12} erg (Blanksby & Ellison 2003), and the rotational partition function for H_2 is given by

$$z_r = \frac{1}{2}\sum_{l=0}^{\infty}(2l + 1)e^{-l(l+1)\Theta_{rot}/T}, \tag{19}$$

which in the limit of $T \gg \Theta_{rot}$ can be approximated as $z_r = T/(2\Theta_{rot})$, where Θ_{rot} = 85.4 K (Hill 1986). The pressure at which a given value of χ_{H_2} is reached at temperature T is

$$P(\chi_{H_2}, T) = 1.6 \times 10^6 \text{ erg cm}^{-3} \times \frac{\chi_{H_2}}{(1 - \chi_{H_2})^2} T^{3/2} \exp\left(-\frac{5.4 \times 10^4 \text{ K}}{T}\right). \tag{20}$$

Contours of χ_{H_2} in the temperature–pressure plane are shown in Figure 13. For $T \lesssim 2000$ K the envelope (pressure range $\approx 10^3$–10^8 erg cm^{-3}) is molecular, but for higher temperatures, atomic hydrogen must be included.

The entropy per particle of hydrogen and helium is

$$\frac{s_{H_2}}{k_B} = \frac{7}{2} + \ln\left(\frac{n_{Q,H_2}}{n_{H_2}}\right) + \ln\left(\frac{T}{2\Theta_{rot}}\right) \tag{21}$$

$$\frac{s_i}{k_B} = \frac{5}{2} + \ln\left(\frac{n_{Q,i}}{n_i}\right), \quad i = \text{H, He}. \tag{22}$$

We use the fact that the temperature is low enough so that the vibrational degrees of freedom of molecular hydrogen, which has a vibrational temperature Θ_{vib} = 6210 K (Hill 1986), are not excited. The entropy per baryon $S_i = s_i/\mu_i$ is then

$$S_{H_2}/k_B = \frac{1}{2}\left(20.8 + \frac{5}{2}\ln T_3 - \ln\rho_{-5}\right), \tag{23}$$

$$S_H/k_B = \left(16.3 + \frac{3}{2}\ln T_3 - \ln\rho_{-5}\right), \tag{24}$$

$$S_{He}/k_B = \frac{1}{4}\left(19.8 + \frac{3}{2}\ln T_3 - \ln\rho_{-5}\right), \tag{25}$$

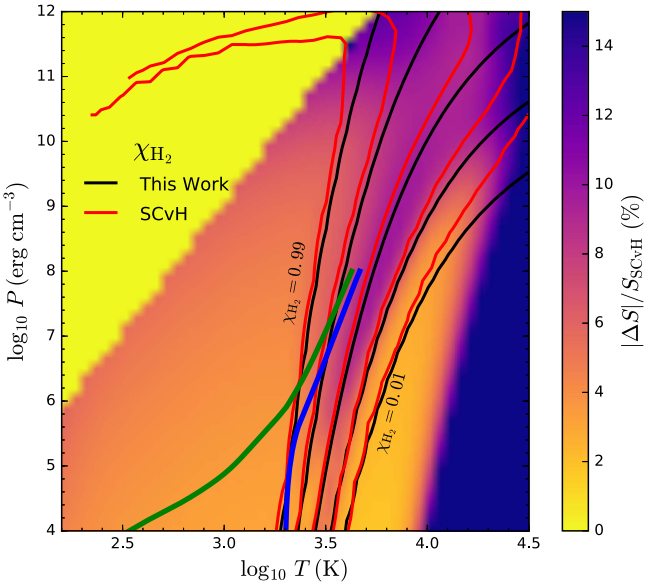

Figure 13. Comparison between the entropy calculated using Equation (26) and that of Saumon et al. (1995), S_{SCvH}. The black and red lines indicate values of constant $\chi_{H_2}(P, T)$ obtained using Equation (18) and from Saumon et al. (1995), respectively, for χ_{H_2} = 0.01, 0.1, 0.5, 0.9, and 0.99. The thick blue and green lines show envelope models from Figure 2 with surface temperatures of 2000 K and 150 K, respectively. There are no SCvH entropy data in the upper left yellow region.

where $T_3 \equiv T/1000$ K and $\rho_{-5} \equiv \rho/(10^{-5}$ g cm$^{-3})$. The total entropy per baryon is

$$S/k_B = \frac{(1 - Y)}{(1 + \chi_{H_2})}[2\chi_{H_2} S_{H_2} + (1 - \chi_{H_2})S_H] + YS_{He} + S_{mix}, \tag{26}$$

where S_{mix} is the entropy of mixing (Saumon et al. 1995) given by

$$S_{mix} = \frac{1}{\mu}(-x_H \ln x_H - x_{H_2} \ln x_{H_2} - x_{He} \ln x_{He}), \tag{27}$$

and the number fractions are

$$x_H = \frac{(1 - Y)(1 - \chi_{H_2})}{(1 + \chi_{H_2})}\mu,\ x_{H_2} = \frac{(1 - Y)(2\chi_{H_2})}{(1 + \chi_{H_2})}\frac{\mu}{2},\ x_{He} = Y\frac{\mu}{4}. \tag{28}$$

Considering the limit of purely molecular hydrogen ($\chi_{H_2} = 1$), we find $\mu = 2.28$, $S_{mix} = 0.18$ and the entropy is given by

$$\frac{S}{k_B/m_p} = 8.80 + 3.38\log_{10}T_3 - 1.01\log_{10}\left(\frac{P}{10^6 \text{ erg cm}^{-3}}\right), \tag{29}$$

having used the ideal gas equation of state to rewrite the density in terms of the temperature and pressure. In the other limit of purely atomic hydrogen ($\chi_{H_2} = 0$), we find $\mu = 1.23$, $S_{mix} = 0.22$ and

$$\frac{S}{k_B/m_p} = 13.47 + 4.68\log_{10}T_3 - 1.87\log_{10}\left(\frac{P}{10^6 \text{ erg cm}^{-3}}\right). \tag{30}$$

From Equations (29) and (30) we can read off the adiabatic index $\nabla_{\rm ad} = (\partial \ln T/\partial \ln P)_S = 0.30$ for the molecular case and $\nabla_{\rm ad} = 0.40$ for the atomic case.

In Figure 13 we show how the results of the above equations compare to the values found in Saumon et al. (1995) (SCvH). The blue and green curves, which show envelope models calculated in Section 3.2, are mostly in a region where the deviation from SCvH is only $|\Delta S|/S_{\rm SCvH} \approx 2\%$–$5\%$. However, farther into the envelope at higher pressures, the error increases to $\sim$10% and so the more detailed equation-of-state tables from SCvH are required. Large deviations are seen for $T \gtrsim 10^4$ K, where atomic hydrogen is ionized, but this region is not relevant for our envelope models. At lower temperatures, the largest deviations from SCvH occur where $\chi_{\rm H_2}$ is transitioning from 0 to 1. Even though our calculation of $\chi_{\rm H_2}$ agrees well with that of SCvH (black and red contours in Figure 13), the small differences in $\chi_{\rm H_2}$ are amplified in the total entropy because atomic hydrogen gives a much larger contribution to entropy than molecular.

APPENDIX B
ENVELOPE WITH POWER-LAW OPACITY

We present here analytic solutions for the accreting envelope that clarify why accreting envelopes have a minimum luminosity. We assume a power-law opacity of the form $\kappa = \kappa_0 P^\alpha T^\beta$. The equations giving the profile of T and P in the envelope are then

$$\frac{dT}{dP} = \frac{3\kappa_0 P^\alpha L}{16\pi acGMT^{3-\beta}} \tag{31}$$

$$\frac{dL}{dP} = \frac{\dot{M} c_P T_0}{P}(\nabla - \nabla_{\rm ad}), \tag{32}$$

where in dL/dP we follow Stahler (1988) and assume in the heating term that $T \approx T_0$ is constant in the envelope. Combining Equations (31) and (32) gives a second-order ODE for T,

$$\frac{d^2T}{dP^2} - \frac{\alpha}{P}\frac{dT}{dP} + \frac{(3-\beta)}{T}\left(\frac{dT}{dP}\right)^2 = \frac{3\kappa_0 P^\alpha}{16\pi acGMT^{3-\beta}}\frac{\dot{M} c_P T_0}{P}(\nabla - \nabla_{\rm ad}). \tag{33}$$

Written in terms of gradients of ∇, this is

$$\frac{d\nabla}{d\ln P} = (\alpha+1)\nabla - (4-\beta)\nabla^2 + \gamma(\nabla - \nabla_{\rm ad}), \tag{34}$$

where we define the coefficient γ as

$$\gamma = \frac{3\kappa_0 P^{1+\alpha}}{16\pi acGMT^{4-\beta}}\dot{M} c_P T_0. \tag{35}$$

Arras & Bildsten (2006) wrote down Equation (34) for nonaccreting envelopes, in which case $\dot{M} = 0$ and $\gamma = 0$. Starting at low pressure where $\nabla \ll 1$, and assuming $\beta < 4$ so that the nonlinear term is negative,[9] the solution is that ∇ increases with increasing pressure at first, but eventually saturates at the limiting value

$$\nabla_\infty = \frac{1+\alpha}{4-\beta}. \tag{36}$$

The gradient ∇_∞ is the radiative zero gradient, for which the first and second terms on the right-hand side of Equation (34) cancel and $d\nabla/dP = 0$. Arras & Bildsten (2006) pointed out that the envelope will only become convective at depth if ∇ can exceed $\nabla_{\rm ad}$, i.e., if $\nabla_\infty > \nabla_{\rm ad}$ (so that for example a constant opacity envelope will not become convective since $\nabla_\infty = 1/4 < \nabla_{\rm ad}$).

Equation (34) has a second root for which $d\nabla/dP = 0$, an isothermal envelope with $\nabla = 0$. However, an important difference is that unlike the root $\nabla = \nabla_\infty$, the isothermal solution $\nabla = 0$ is unstable. If ∇ is slightly larger than zero, it will increase with pressure and approach the stable solution $\nabla = \nabla_\infty$. If ∇ is slightly lower than zero, it will become more and more negative with increasing pressure, $\nabla \to -\infty$. This is illustrated in the left-hand panel of Figure 14, which shows the behavior for several different starting values of ∇.

To understand what happens when accretion is included, we consider the case where the coefficient γ is a constant (in fact γ will be an increasing function of depth for $\nabla < \nabla_\infty$, but we expect this would not qualitatively change the argument). Then setting $d\nabla/d\ln P = 0$ gives

$$(4-\beta)\nabla^2 - (1+\alpha+\gamma)\nabla + \gamma\nabla_{\rm ad} = 0 \tag{37}$$

or

$$\nabla = \frac{1+\alpha+\gamma}{4-\beta}\left[\frac{1}{2} \pm \frac{1}{2}\left(1 - \frac{4(4-\beta)\gamma\nabla_{\rm ad}}{(1+\alpha+\gamma)^2}\right)^{1/2}\right]. \tag{38}$$

If we define a modified $\tilde{\nabla}_\infty = (1+\alpha+\gamma)/(4-\beta)$, then this is

$$\nabla = \tilde{\nabla}_\infty\left[\frac{1}{2} \pm \frac{1}{2}\left(1 - \frac{4\gamma\nabla_{\rm ad}}{(1+\alpha+\gamma)\tilde{\nabla}_\infty}\right)^{1/2}\right]. \tag{39}$$

Again we see that there are two roots; for $\gamma \ll 1$ they are

$$\nabla_1 \approx \tilde{\nabla}_\infty, \qquad \nabla_2 \approx \frac{\gamma\nabla_{\rm ad}}{1+\alpha}. \tag{40}$$

The effect of accretion is to make the unstable root ∇_2 nonzero. An envelope with $\nabla > \nabla_2$ at low pressure will evolve in a stable way: with increasing pressure, ∇ will increase until it reaches the asymptotic value $\nabla = \nabla_1$ (or until it becomes convective and Equation (31) no longer applies). However, if $0 < \nabla < \nabla_2$, then ∇ diverges unstably away from ∇_2, decreasing with depth and eventually becoming negative, corresponding to a temperature profile that reaches a maximum and then declines with depth. This is shown in the right-hand panel of Figure 14 and matches the behavior we see in our numerical envelope integrations in Section 2 at low luminosity. The luminosity corresponding to the minimum gradient ∇_2 is (from Equation (31) and using Equation (35) for γ)

$$L_{\rm min} = \frac{16\pi acGMT^4}{3\kappa P}\frac{\gamma}{1+\alpha}\nabla_{\rm ad} = \dot{M} c_P T_0 \frac{\nabla_{\rm ad}}{1+\alpha}, \tag{41}$$

which is tens of percent of the compressional heating luminosity (see Equation (22) of Stahler 1988 for a similar result).

[9] For realistic opacities, we find that $\beta > 4$ for some regions of the temperature–pressure plane relevant for our envelope models. When $\beta > 4$, the nonlinear term in Equation (34) changes sign, and the stable root $\nabla_\infty < 0$. A nonaccreting envelope with outward flux $\nabla > 0$ at the surface will then always become convective because ∇ rapidly increases inwards. The effect of accretion—to move the isothermal root ∇_2 to a low positive value—is the same whether β is smaller or larger than 4. One difference is that a solution with $0 < \nabla < \nabla_2$ at low pressure will eventually go to the stable point $\nabla \to \nabla_1 < 0$ rather than diverging to $\nabla \to -\infty$. We have also checked the value of α from realistic opacities and find $\alpha > -1$ always, so that the linear term in Equation (34) is positive.

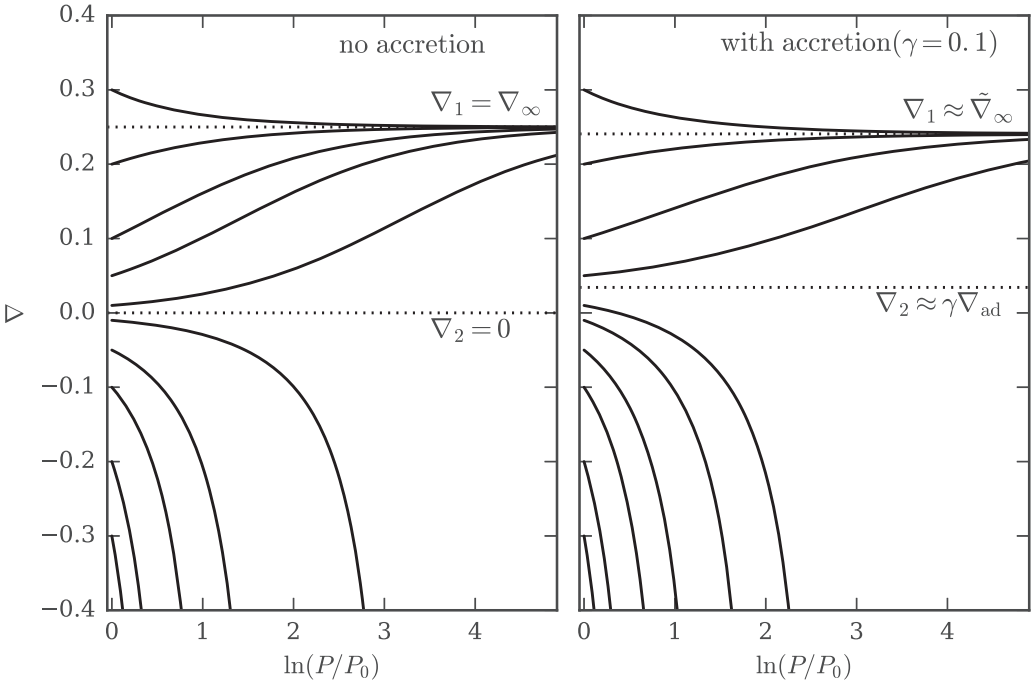

Figure 14. Integrations of Equation (34) for a constant opacity ($\alpha = 0$, $\beta = 0$) and $\nabla_{\rm ad} = 0.33$, for different initial values $\nabla = \pm 0.01, \pm 0.05, \pm 0.1, \pm 0.2$, and ± 0.3 at $P = P_0$. The dotted horizontal lines show the roots ∇_1 and ∇_2 where $d\nabla/d\ln P = 0$. The left panel shows the result with no accretion ($\gamma = 0$). The radiative zero slope ∇_∞ is a stable point; the isothermal slope $\nabla = 0$ is unstable. The right panel shows the result with accretion ($\gamma = 0.1$). The unstable point now shifts away from zero, becoming $\nabla_2 \approx \gamma \nabla_{\rm ad} > 0$, corresponding to a minimum luminosity in the envelope.

REFERENCES

Arras, P., & Bildsten, L. 2006, ApJ, 650, 394
Bailey, V., Meshkat, T., Reiter, M., et al. 2014, ApJL, 780, L4
Baraffe, I., Chabrier, G., Barman, T. S., Allard, F., & Hauschildt, P. H. 2003, A&A, 402, 701
Baraffe, I., Chabrier, G., & Gallardo, J. 2009, ApJL, 702, L27
Baraffe, I., Vorobyov, E., & Chabrier, G. 2012, ApJ, 756, 118
Blanksby, S. J., & Ellison, G. B. 2003, AcChR, 36, 255
Bodenheimer, P., Hubickyj, O., & Lissauer, J. J. 2000, Icar, 143, 2
Bonnefoy, M., Boccaletti, A., Lagrange, A.-M., et al. 2013, A&A, 555, A107
Bowler, B. P. 2016, PASP, 128, 968
Bowler, B. P., Liu, M. C., Shkolnik, E. L., & Dupuy, T. J. 2013, ApJ, 774, 55
Burrows, A., Guillot, T., Hubbard, W. B., et al. 2000, ApJL, 534, L97
Burrows, A., Marley, M., Hubbard, W. B., et al. 1997, ApJ, 491, 856
Calvet, N., & Gullbring, E. 1998, ApJ, 509, 802
Chabrier, G., Johansen, A., Janson, M., & Rafikov, R. 2014, Protostars and Planets VI
Chauvin, G. 2004, A&A, 425, L25
Chen, H., & Rogers, L. A. 2017, ApJ, 831, 180
Commerçon, B., Audit, E., Chabrier, G., & Chièze, J.-P. 2011, A&A, 530, A13
Currie, T., Burrows, A., Madhusudhan, N., et al. 2013, ApJ, 776, 15
Currie, T., Cloutier, R., Brittain, S., et al. 2015, ApJL, 814, L27
Currie, T., Daemgen, S., Debes, J., et al. 2014a, ApJL, 780, L30
Currie, T., Muto, T., Kudo, T., et al. 2014b, ApJL, 796, L30
D'Orazi, V., Desidera, S., Gratton, R., et al. 2016, arXiv:1609.02530
Ferguson, J. W., Alexander, D. R., Allard, F., et al. 2005, ApJ, 623, 585
Fortney, J. J., Marley, M. S., Hubickyj, O., Bodenheimer, P., & Lissauer, J. J. 2005, AN, 326, 925
Fortney, J. J., Marley, M. S., Saumon, D., & Lodders, K. 2008, ApJ, 683, 1104
Freedman, R. S., Lustig-Yaeger, J., Fortney, J. J., et al. 2014, ApJS, 214, 25
Freedman, R. S., Marley, M. S., & Lodders, K. 2008, ApJS, 174, 504
Fuhrmann, K., & Chini, R. 2015, ApJ, 806, 163
Garufi, A., Quanz, S. P., Schmid, H. M., et al. 2016, A&A, 588, A8
Hartmann, L., Cassen, P., & Kenyon, S. J. 1997, ApJ, 475, 770
Helled, R., Bodenheimer, P., Podolak, M., et al. 2014, in Protostars and Planets VI, ed. H. Beuther et al. (Tucson, AZ: Univ. Arizona Press), 643
Henyey, L., Vardya, M. S., & Bodenheimer, P. 1965, ApJ, 142, 841
Hill, T. L. 1986, An Introduction to Statistical Thermodynamics (New York: Dover)
Huang, X., & Cumming, A. 2012, ApJ, 757, 47
Hubeny, I., & Mihalas, D. 2014, in Theory of Stellar Atmospheres, ed. I. Hubeny & D. Mihalas (Princeton, NJ: Princeton Univ. Press)
Hubickyj, O., Bodenheimer, P., & Lissauer, J. J. 2005, Icar, 179, 415
Kuzuhara, M., Tamura, M., Kudo, T., et al. 2013, ApJ, 774, 11
Lagrange, A. M. 2009, A&A, 506, 927
Lagrange, A. M. 2010, Sci, 329, 57
Leconte, J., & Chabrier, G. 2012, A&A, 540, A20
Lissauer, J. J., Hubickyj, O., D'Angelo, G., & Bodenheimer, P. 2009, Icar, 199, 338
Lovelace, R. V. E., Covey, K. R., & Lloyd, J. P. 2011, AJ, 141, 51
Macintosh, B., Graham, J. R., Barman, T., et al. 2015, Sci, 350, 64
Marleau, G.-D., & Cumming, A. 2014, MNRAS, 437, 1378
Marleau, G.-D., Klahr, H., Mordasini, C., & Kuiper, R. 2016, ApJ, submitted
Marley, M. S., Fortney, J. J., Hubickyj, O., Bodenheimer, P., & Lissauer, J. J. 2007, ApJ, 655, 541
Marois, C. 2008, Sci, 322, 1348
Marois, C., Zuckerman, B., Konopacky, Q. M., Macintosh, B., & Barman, T. 2010, Natur, 468, 1080
Mordasini, C. 2013, A&A, 558, A113
Mordasini, C. 2014, A&A, 572, A118
Mordasini, C., Alibert, Y., Klahr, H., & Henning, T. 2012, A&A, 547, A111
Mordasini, C., Klahr, H., Alibert, Y., Miller, N., & Henning, T. 2014, A&A, 566, A141
Mordasini, C., Mollière, P., Dittkrist, K.-M., Jin, S., & Alibert, Y. 2015, IJAsB, 14, 201
Movshovitz, N., Bodenheimer, P., Podolak, M., & Lissauer, J. J. 2010, Icar, 209, 616
Movshovitz, N., & Podolak, M. 2008, Icar, 194, 368
Nettelmann, N., Fortney, J. J., Moore, K., & Mankovich, C. 2015, MNRAS, 447, 3422
Neuhäuser, R., & Schmidt, T. O. B. 2012, arXiv:1201.3537
Ormel, Ch. 2014, ApJL, 789, L18
Owen, J. E., & Menou, K. 2016, ApJL, 819, L14
Paxton, B., Bildsten, L., Dotter, A., et al. 2011, ApJS, 192, 3
Paxton, B., Cantiello, M., Arras, P., et al. 2013, ApJS, 208, 4
Paxton, B., Marchant, P., Schwab, J., et al. 2015, ApJS, 220, 15
Podolak, M. 2003, Icar, 165, 428
Pollack, J. B., Hubickyj, O., Bodenheimer, P., et al. 1996, Icar, 124, 62
Prialnik, D., & Livio, M. 1985, MNRAS, 216, 37
Quanz, S. P. 2015, ApJ, 807, 64
Quanz, S. P., Amara, A., Meyer, M. R., et al. 2013, ApJL, 766, L1

Rameau, J., Chauvin, G., & Lagrange, A. M. 2013, ApJL, 772, L15
Sallum, S., Follette, K. B., Eisner, J. A., et al. 2015, Natur, 527, 342
Saumon, D., Chabrier, G., & van Horn, H. M. 1995, ApJS, 99, 713
Semenov, D., Henning, T., Helling, C., Ilgner, M., & Sedlmayr, E. 2003, A&A, 410, 611
Siess, L., Forestini, M., & Bertout, C. 1997, A&A, 326, 1001
Spiegel, D. S., & Burrows, A. 2012, ApJ, 745, 174
Stahler, S. W. 1988, ApJ, 332, 804
Stahler, S. W., Shu, F. H., & Taam, R. E. 1980, ApJ, 241, 637
Stevenson, D. J. 1982, P&SS, 30, 755
Szulágyi, J., & Mordasini, C. 2016, arXiv:1609.08652
Todorov, K. O., Luhman, K. L., Konopacky, Q. M., et al. 2014, ApJ, 788, 40
Wagner, K., Apai, D., Kasper, M., et al. 2016, Sci, 353, 673
Wu, Y., & Lithwick, Y. 2013, ApJ, 763, 13